Chemical Differentiation around Five Massive Protostars Revealed by ALMA: Carbon-chain Species and Oxygen/Nitrogen-bearing Complex Organic Molecules

Kotomi Taniguchi[1] , Liton Majumdar[2,3] , Paola Caselli[4] , Shigehisa Takakuwa[5,6] , Tien-Hao Hsieh[4] , Masao Saito[1,7] , Zhi-Yun Li[8] , Kazuhito Dobashi[9] , Tomomi Shimoikura[10] , Fumitaka Nakamura[1,7,11] , Jonathan C. Tan[8,12] , and Eric Herbst[8,13]

[1] National Astronomical Observatory of Japan, National Institutes of Natural Sciences, 2-21-1 Osawa, Mitaka, Tokyo 181-8588, Japan; kotomi.taniguchi@nao.ac.jp
[2] School of Earth and Planetary Sciences, National Institute of Science Education and Research, Jatni 752050, Odisha, India
[3] Homi Bhabha National Institute, Training School Complex, Anushaktinagar, Mumbai 400094, India
[4] Max-Planck-Institut für Extraterrestrische Physik, Gießenbachstrasse 1, D-85741 Garching bei München, Germany
[5] Department of Physics and Astronomy, Graduate School of Science and Engineering, Kagoshima University, 1-21-35 Korimoto, Kagoshima, Kagoshima 890-0065, Japan
[6] Academia Sinica Institute of Astronomy and Astrophysics, 11F of Astro-Math Bldg., 1, Section 4, Roosevelt Road, Taipei 10617, Taiwan
[7] Department of Astronomical Science, School of Physical Science, SOKENDAI (The Graduate University for Advanced Studies), Osawa, Mitaka, Tokyo 181-8588, Japan
[8] Department of Astronomy, University of Virginia, Charlottesville, VA 22904, USA
[9] Department of Astronomy and Earth Sciences, Tokyo Gakugei University, Nukuikitamachi, Koganei, Tokyo 184-8501, Japan
[10] Faculty of Social Information Studies, Otsuma Women's University, Sanban-cho, Chiyoda, Tokyo 102-8357, Japan
[11] Department of Astronomy, Graduate School of Science, The University of Tokyo, Hongo, Bunkyo, Tokyo 113-0033, Japan
[12] Department of Space, Earth & Environment, Chalmers University of Technology, SE-412 93 Gothenburg, Sweden
[13] Department of Chemistry, University of Virginia, Charlottesville, VA 22904, USA

Abstract

We present Atacama Large Millimeter/submillimeter Array Band 3 data toward five massive young stellar objects (MYSOs), and investigate relationships between unsaturated carbon-chain species and saturated complex organic molecules (COMs). An HC_5N ($J = 35-34$) line has been detected from three MYSOs, where nitrogen (N)-bearing COMs (CH_2CHCN and CH_3CH_2CN) have been detected. The HC_5N spatial distributions show compact features and match with a methanol (CH_3OH) line with an upper-state energy around 300 K, which should trace hot cores. The hot regions are more extended around the MYSOs where N-bearing COMs and HC_5N have been detected compared to two MYSOs without these molecular lines, while there are no clear differences in the bolometric luminosity and temperature. We run chemical simulations of hot-core models with a warm-up stage, and compare with the observational results. The observed abundances of HC_5N and COMs show good agreements with the model at the hot-core stage with temperatures above 160 K. These results indicate that carbon-chain chemistry around the MYSOs cannot be reproduced by warm carbon-chain chemistry, and a new type of carbon-chain chemistry occurs in hot regions around MYSOs.

1. Introduction

Astrochemical studies have revealed that chemical composition reflects evolutionary stages, physical conditions, and star formation processes (see, e.g., Caselli & Ceccarelli 2012; Jørgensen et al. 2020 for a review). The most classical scenario is that unsaturated carbon-chain species (e.g., C_nH, cyanopolyynes ($HC_{2n+1}N$), C_nS) are efficiently formed mainly by gas-phase ion–molecule reactions in the early starless-core stage (e.g., Herbst & Leung 1989; Suzuki et al. 1992). These carbon-chain species were considered to be deficient in more evolved protostellar stages, because they are destroyed by reactions with ions and atomic oxygen or adsorbed onto dust grains in dense, cold prestellar cores. Thus, the carbon-chain species have been considered to be good chemical evolutionary indicators for the early stages of star formation processes, and known as "early-type species" (Suzuki et al. 1992; Benson et al. 1998).

In contrast to the above classical scenario of carbon-chain species, a few carbon-chain-rich low-mass protostars have been discovered (Sakai et al. 2008), and chemical diversity was found around low-mass young stellar objects (YSOs). The carbon-chain molecules around low-mass YSOs are formed by the initial reaction between CH_4, which sublimates from dust grains in lukewarm envelopes ($\approx$25–30 K), and C^+ (Hassel et al. 2008). Such a carbon-chain formation mechanism was named warm carbon-chain chemistry (WCCC; Sakai et al. 2008).

After the discovery of WCCC, several survey observations focusing on both carbon-chain species and saturated complex organic molecules (COMs)[14] were conducted toward low-mass star-forming regions using single-dish telescopes. Graninger et al. (2016) conducted survey observations of CH_3OH and C_4H with the IRAM 30 m telescope. These observations revealed that these two species are positively correlated, indicating that carbon-chain species and COMs can coexist around low-mass YSOs. Furthermore, they found a tentative correlation between

---

[14] COMs or iCOMs are defined as molecules consisting of more than six atoms (Herbst & van Dishoeck 2009).

the gas-phase C_4H/CH_3OH abundance ratio and the CH_4/CH_3OH abundance ratio in ice, which supports the WCCC mechanism starting with sublimation of CH_4 (Hassel et al. 2008). Higuchi et al. (2018) found that the CCH/CH_3OH column density ratios differ by two orders of magnitude among the observed protostellar cores, and suggested that YSOs with higher CCH/CH_3OH column density ratios are possibly located near cloud edges or in isolated clouds. These survey observations indicate the chemical diversity around low-mass YSOs. Lindberg et al. (2017) conducted observations of H_2CO and *cyclic*–C_3H_2 (c–C_3H_2) toward the Ophiuchus star-forming region using the APEX 12 m telescope, and suggested that c–C_3H_2 exists in more shielded parts of envelopes, while the H_2CO line traces mainly outer irradiated envelopes. On the other hand, high-angular-resolution observations toward two low-mass YSOs in the Ophiuchus region with the Atacama Large Millimeter/submillimeter Array (ALMA) revealed that c–C_3H_2 is enhanced in regions irradiated by the UV radiation from a nearby Herbig Be star, while the H_2CO and CH_3OH emission comes from shielded regions (Taniguchi et al. 2021b). Thus, analyses of spatially resolved data are necessary to investigate the relationships between carbon-chain species and COMs around YSOs. These studies regarding the relations between carbon-chain species and COMs have progressed in nearby low-mass star-forming regions, whereas the chemical diversity in high-mass star-forming regions is still unclear.

Thanks to the development of the radio interferometers, including ALMA, astrochemical studies in high-mass star-forming regions have proceeded significantly. Most astrochemical studies toward massive young stellar objects (MYSOs) have focused on COMs, namely hot-core chemistry (e.g., Csengeri et al. 2019; Taniguchi et al. 2020; Gorai et al. 2021; Qin et al. 2022). Regarding observations of carbon-chain species toward high-mass star-forming regions, on the other hand, single-dish surveys have been undertaken. For example, Rivilla et al. (2020) conducted survey observations toward 28 high-mass star-forming cores to investigate deuterium fractionation of HC_3N, but they could not find any significant trends with the evolutionary stages or the kinetic temperatures, which are possibly caused by low angular resolution (ang. res.). Taniguchi et al. (2018c, 2019b) conducted survey observations of carbon-chain species and N_2H^+ toward high-mass starless cores and high-mass protostellar objects (HMPOs). The N_2H^+/HC_3N abundance ratio is found to decrease as cores evolve, and is suggested to be an evolutionary indicator for the early stages of high-mass star-forming regions (Taniguchi et al. 2019b). This downward trend of the N_2H^+/HC_3N ratio is explained by destruction of N_2H^+ by reactions with CO, and formation of HC_3N from CH_4 and/or C_2H_2. These key species (CO, CH_4, C_2H_2) can sublimate from dust grains around 20 K, 25 K, and 50 K, respectively. These results indicate that HC_3N forms efficiently and ubiquitously around HMPOs or young high-mass stars embedded in dense gas and dust. In addition, the detection rate of HC_5N around HMPOs is found to be 50%, which is almost consistent with previous surveys toward hot cores associated with 6.7 GHz CH_3OH masers (Green et al. 2014). These results suggest the presence of two chemically different envelopes around MYSOs: hot-core type and carbon-chain-rich type, which may be an analog of the chemical diversity found around low-mass YSOs (hot corino versus WCCC). However, the detected HC_5N lines with low upper-state energies are likely to come from outer cold envelopes, not from inner warm envelopes or hot-core regions; and then their observational results are not enough to confirm that carbon-chain species exist around MYSOs.

A few observations have focused on the relationships between carbon-chain species and COMs around MYSOs by single-dish observations (Taniguchi et al. 2017, 2018b). However, as these observations were conducted using single-dish telescopes, they could not reveal the spatial distributions of these carbon-chain species around MYSOs. Observations using the Very Large Array (VLA) revealed the spatial distributions of cyanopolyynes (HC_3N, HC_5N, and HC_7N) in the *Ka* band (36 GHz) toward the MYSO G28.28-0.36, which is known as a carbon-chain-rich/COM-poor MYSO (Taniguchi et al. 2018b). They found that cyanopolyynes are associated with 450 μm continuum clumps that likely contain deeply embedded low- or intermediate-mass YSOs (Taniguchi et al. 2018a). Thus, they could not investigate the spatial distributions just around MYSOs using lines of cyanopolyynes in the *Ka* band. We need to observe higher upper-state-energy lines, which can be excited in hot gas ($\sim$100 K), to trace hot components of cyanopolyynes.

In this paper, we present ALMA Band 3 data toward five HMPOs taken in Cycle 6. We focus not only on oxygen (O)-bearing and nitrogen (N)-bearing COMs, but also on carbon-chain species, especially cyanopolyynes ($HC_{2n+1}N$, $n = 1, 2, 3, \ldots$). We will investigate the relationships among these different types of species, and discuss the connections between chemical features and physical conditions of the target sources.

The structure of this paper is as follows. We describe archival data sets and the reduction procedure in Section 2. In Sections 3.1 and 3.2, continuum images and moment 0 maps of the observed molecular species are presented. We present spectral analyses in Section 3.3. We compare spatial distributions among different types of molecules to investigate the chemical differentiation among each source in Section 4.1. Chemical composition is compared among each core and the relationships between the chemistry and physical conditions are discussed in Section 4.2. Comparisons of chemical composition between observational results and chemical simulations will be discussed in Section 4.3. In Section 5, the main conclusions of this paper are summarized.

2. Data Reduction

We have analyzed the ALMA Band 3 data toward five HMPOs.[15] Details of the observations of this project are described in Gieser et al. (2023). Details about the five target sources and molecular lines presented in this paper are summarized in Tables 1 and 2, respectively. The data sets consist of six scheduling blocks. Table 3 summarizes the information on each data set. These data sets were obtained with three different frequency setups, corresponding to each column of Table 3. The data toward G9.62+0.19, G10.47+0.03, and G12.89+0.49 are contained in the same scheduling blocks (the upper rows of Table 3), and the other two sources, G16.57-0.05 and G19.88-0.53, are involved in the other scheduling blocks (the lower rows of Table 3). The observations of each scheduling block were conducted with different baselines because of the different observing dates. As a result, the ang.

Table 1
Summary of Target Sources

Source	R.A. (J2000)	Decl. (J2000)	D[a] (kpc)	$V_{\rm lsr}$ (km s^{-1})	$L_{\rm bol}$[a] ($L_\odot$)	$M_{\rm clump}$[a] ($M_\odot$)	$N({\rm H_2})$[a] (cm^{-2})	$T_{\rm dust}$[a] (K)
G9.62+0.19	$18^{\rm h}\,06^{\rm m}\,14\overset{s}{.}9$	$-20°31'39\overset{''}{.}2$	5.2	4.4	2.39×10^5	3.33×10^3	1.64×10^{23}	32
G10.47+0.03	$18^{\rm h}\,08^{\rm m}\,38\overset{s}{.}2$	$-19°51'50\overset{''}{.}1$	10.7	67.8	4.48×10^5	2.58×10^4	6.35×10^{23}	25
G12.89+0.49	$18^{\rm h}\,11^{\rm m}\,51\overset{s}{.}5$	$-17°31'28\overset{''}{.}9$	3.0	33.8	1.79×10^4	1.26×10^3	1.85×10^{23}	23
G16.57-0.05	$18^{\rm h}\,21^{\rm m}\,09\overset{s}{.}2$	$-14°31'45\overset{''}{.}5$	4.7	59.1	1.82×10^4	1.34×10^3	1.05×10^{23}	25
G19.88-0.53	$18^{\rm h}\,29^{\rm m}\,14\overset{s}{.}7$	$-11°50'24\overset{''}{.}0$	3.3	43.6	7.89×10^3	1.64×10^3	1.82×10^{23}	20

Note.
[a] Taken from Urquhart et al. (2018).

Table 2
Summary of Molecular Lines for Moment 0 Maps

Species	Transition	Frequency[a] (GHz)	$E_{\rm up}/k$ (K)
SiO	$2-1$	86.84696	6.3
Ethynyl (CCH)	$N = 1 - 0, J = \frac{3}{2} - \frac{1}{2}, F = 2 - 1$	87.316925	4.2
Isocyanic acid (HNCO)	$4_{0,4}-3_{0,3}$	87.925237	10.5
Cyanoacetylene (HC$_3$N)	$10-9$	90.979023	24.0
Methyl cyanide (CH$_3$CN)	5_3-4_3	91.9711307	77.5
Vinyl cyanide (CH$_2$CHCN)	$10_{1,10}-9_{1,9}$	92.42625	26.6
Cyanodiacetylene (HC$_5$N)	$35-34$	93.188123	80.5
Methanol (CH$_3$OH)	$1_{0,1}-2_{1,2}, v_t = 1$	93.196673	302.9
Ethyl cyanide (CH$_3$CH$_2$CN)	$11_{0,11}-10_{0,10}$	96.919762	28.1
SO	3_2-2_1	99.29987	9.2
Dimethyl ether (CH$_3$OCH$_3$)[b]	$4_{1,4}-3_{0,3}$ (EA, AE, EE, AA)	99.324362–99.326072	10.2

Notes.
[a] Rest frequencies were taken from the Cologne Database for Molecular Spectroscopy (CDMS; Müller et al. 2005). Papers of spectroscopic laboratory experiments are listed in the CDMS website.
[b] Four lines are blended.

Table 3
Information on Data Sets Presented in This Paper

	First Setup	Second Setup	Third Setup
Frequency range	96.06–110.43 GHz	86.28–100.79 GHz	90.20–105.61 GHz
Contained lines	Continuum	CCH, CH$_3$OCH$_3$, HNCO, CH$_3$CH$_2$CN, SiO, SO	HC$_5$N, HC$_3$N, CH$_3$OH CH$_3$CN, CH$_2$CHCN
G9.62+0.19, G10.47+0.03, G12.89+0.49			
12 m array observations	2019 May 3	2018 Nov 20	2019 Jan 10
Projected baseline distance	12.0 m–673.0 m	15.1 m–1.4 km	12.0 m–269.2 m
Typical ang. res.	$1\overset{''}{.}8 \times 1\overset{''}{.}0$	$0\overset{''}{.}8 \times 0\overset{''}{.}8$	$4\overset{''}{.}5 \times 2\overset{''}{.}5$
7 m array observations	2019 Jan 26, Mar 29	2019 May 10, 20, 23	2019 May 20, 23
G16.57-0.05, G19.88-0.53			
12 m array observations	2019 Apr 17	2018 Nov 16, 19	2018 Oct 30
Projected baseline distance	12.0 m–782.9 m	12.6 m–1.4 km	12.5 m–1.4 km
Typical ang. res.	$1\overset{''}{.}5 \times 1\overset{''}{.}0$	$1\overset{''}{.}0 \times 0\overset{''}{.}7$	$1\overset{''}{.}0 \times 0\overset{''}{.}7$
7 m array observations	2019 Apr 1, 17	2019 Jan 16, 17	2019 Jan 16, 19

res. is different among sources and frequency setups. The bandwidth and frequency resolution of the spectral windows for the molecular lines are 117 MHz and 244 kHz, respectively. The frequency resolution corresponds to the velocity resolution of $\sim$0.8 km s^{-1} at the observed frequency.

We conducted data reduction and imaging using the Common Astronomy Software Application (CASA; McMullin et al. 2007) on the pipeline-calibrated visibilities. We ran the calibration scripts using CASA versions 5.4.0 and 5.6.1, according to QA2 reports. The data cubes were created by the *tclean* task in CASA, combining the data of the 12 m and 7 m arrays. Briggs weighting with a robustness parameter of 0.5 was applied. The phase reference centers of each source are summarized in Table 1.

Continuum images ($\lambda = 2.75$ mm) were created from the broadest spectral window (the central frequency of 109.5 GHz and the bandwidth of 1.875 GHz) using the *imcontsub* task in CASA. We determined line-free channels checking the *tclean* images in the *imcontsub* task, because molecular lines have been detected at the continuum core positions.
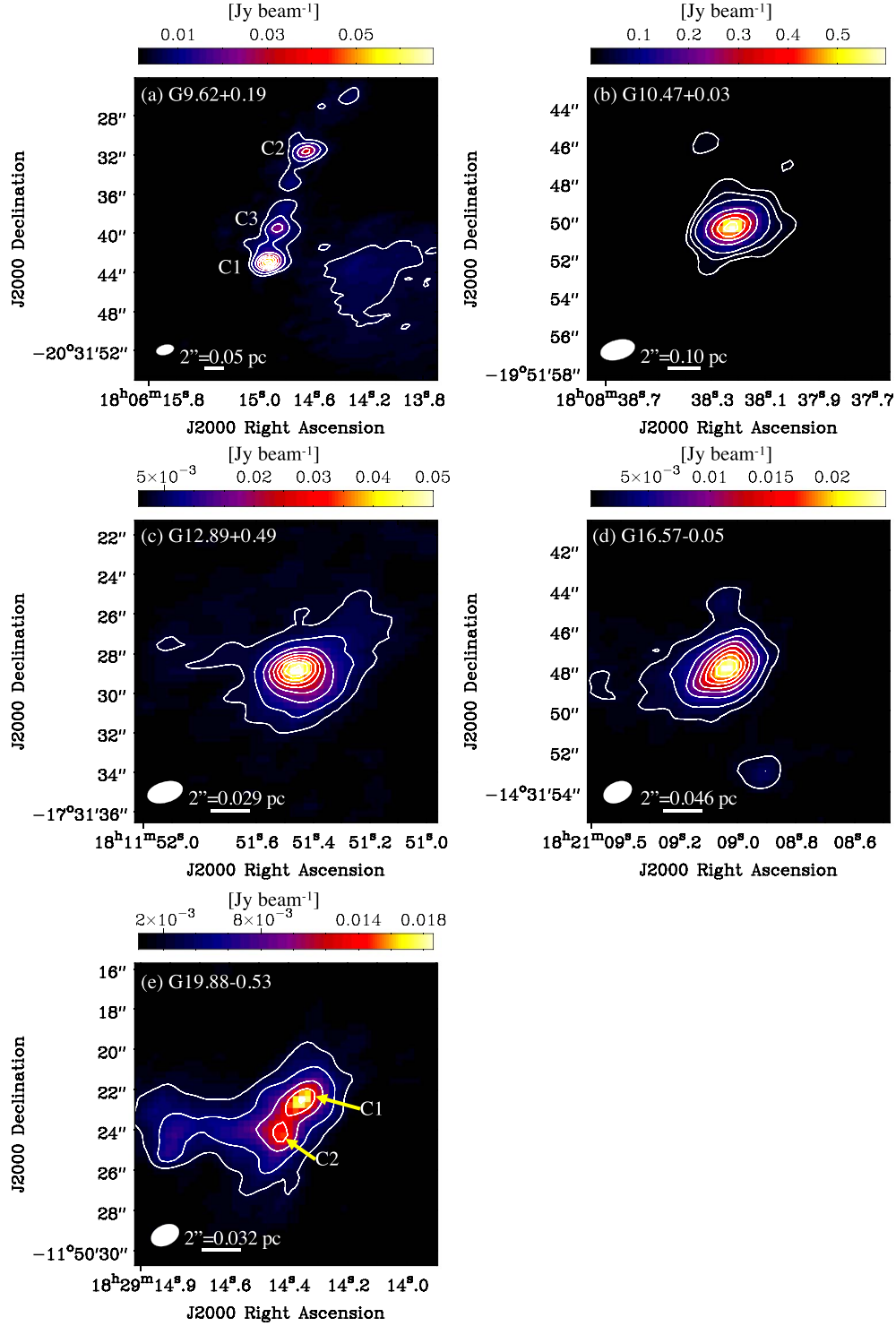
Figure 1. Continuum images ($\lambda = 2.75$ mm, combination of the 12 m and 7 m arrays) toward five sources. The filled white ellipse indicates the angular resolution. Information about the noise level, contour level, and angular resolution for each panel is summarized in Table 4.

3. Results and Analyses

3.1. Continuum Images

Figure 1 shows continuum images ($\lambda = 2.75$ mm) toward the five sources. The ang. res., beam position angle (PA), rms noise level, and contour levels of each continuum image are summarized in Table 4. We applied 2D Gaussian fitting for the continuum images in CASA, and identified cores. Table 5 summarizes the properties of the identified cores. Three and two cores are identified in G9.62+0.19 and G19.88-0.53, respectively. We named them C1, C2, and C3 in the order of peak flux.

In the G9.62+0.19 region, 12 millimeter cores were identified along a filamentary structure in the 1.3 mm continuum emission (Liu et al. 2017). MM1 is located outside of our image. The peaks of Cores C1, C2, and C3 we identified correspond to peak positions of cores MM11, MM4, and MM8, respectively,

Table 4
Information on the Continuum Maps

Panel	Ang. Res.	Beam PA	rms[a]	Contour Level
(a) G9.62+0.19	$1''85 \times 1''04$	$-75°9$	1.0	5, 10–60σ (10σ step)
(b) G10.47+0.03	$1''86 \times 1''04$	$-75°5$	3.0	5, 10, 20–180σ (40σ step)
(c) G12.89+0.49	$1''82 \times 1''04$	$-74°3$	0.6	5, 10–80σ (10σ step)
(d) G16.57-0.05	$1''47 \times 1''00$	$-65°3$	0.3	5, 10–80σ (10σ step)
(e) G19.88-0.53	$1''46 \times 1''00$	$-64°0$	0.45	5, 10–40σ (10σ step)

Note.
[a] Unit is mJy per beam.

identified by Liu et al. (2017). The evolutionary stages of these cores (MM11, MM4, and MM8) were proposed to be a ultracompact H II region (UC H II), a late hot molecular core (HMC), or a hyper-compact H II region (HC H II) and HMC, respectively (Liu et al. 2017).

The morphology of the continuum emission in G10.47+0.03 is different from ALMA Band 4 data drawn at an ang. res. of $\sim$0$''$7 (Gorai et al. 2020). The difference seems to be caused by the beam effect, and the core is unlikely spatially resolved sufficiently, because of the farthest distance (10.7 kpc; Table 1). The weak emission at the northeast position corresponds to a sharp feature in the 1.88 and 2.30 mm continuum images in Figure 1 in Gorai et al. (2020).

The continuum emission of G12.89+0.49 (also known as IRAS 18089-1732) shows an elongated structure from northwest to southeast. This feature is also seen in the 1.2 mm continuum emission (Sanhueza et al. 2021). We identify one core in our data. Even in higher-angular-resolution data (0$''$3, corresponding to 700 au), only one core can be seen (Sanhueza et al. 2021). The morphology of the continuum emission in G16.57-0.05 (also known as IRAS 18182-1433) is consistent with a previous result reported by Qin et al. (2022).

G19.88-0.53 consists of two continuum cores, and the obtained morphology of the continuum image is consistent with that reported by Issac et al. (2020). Cores C1 and C2 correspond to MM2 and MM1, respectively, identified by Issac et al. (2020). Both of the cores are associated with radio emission (Zapata et al. 2006), and a 44 GHz CH$_3$OH maser has been detected at C2 (Rodríguez-Garza et al. 2017). Zapata et al. (2006) suggested that this region is a triple stellar system based on VLA 1.3 cm and 7 mm continuum images. Cores C1 and C2 correspond to IRAS 18264-1152b and IRAS 18264-1152c, respectively (Zapata et al. 2006), but we cannot recognize the third one (IRAS 18264-1152a), which is located at $\sim$2$''$ to the west from the two continuum cores.

3.2. Moment 0 Maps of Molecular Lines

Figures 2–6 show moment 0 maps of molecular lines toward the five sources (combination of the 12 m and 7 m arrays). The lines' information used in these moment 0 maps are summarized in Table 2. Except for G10.47+0.03 (Figure 3), some panels (CCH, HC$_3$N, SiO, and SO) show different scales, because their emission regions are extended. These panels are presented later. The white dashed squares in these panels indicate regions of the other maps showing the zoomed-in images presented earlier. Four lines of CH$_3$OCH$_3$ are not resolved due to very close frequencies. Thus, we made moment 0 maps including all of these lines. Information about ang. res., beam PA, rms noise level, and contour levels is summarized in Table 6. Here, we note that these data sets were obtained on different days (see

Table 3 in Section 2); we will compare the molecular lines observed simultaneously in the following parts of this paper. For instance, CH$_3$OH, HC$_5$N, HC$_3$N, CH$_3$CN, and CH$_2$CHCN can be compared straightforwardly in each source. We confirmed that the peak positions of the continuum emission obtained from the widest frequency band (Figure 1) are consistent with those made from data containing molecular lines (bandwidth 117 MHz) by the *imcontsub* task. We can thus discuss consistency and inconsistency between the peaks of the molecular lines and continuum emission.

All of the molecular lines have been detected in G9.62+0.19 (Figure 2), G10.47+0.03 (Figure 3), and G12.89+0.49 (Figure 4). On the other hand, all of the molecular lines except for HC$_5$N and N-bearing COMs (CH$_2$CHCN and CH$_3$CH$_2$CN) have been detected in G16.57-0.05 (Figure 5) and G19.88-0.53 (Figure 6).

The peak positions of the spatial distribution of the HC$_5$N ($J = 35-34$; $E_{up}/k = 80.5$ K) line are coincident with the continuum peaks shown as white contours in G9.62+0.19, G10.47+0.03, and G12.89+0.49. In G9.62+0.19, the peak of the weaker HC$_5$N emission is not completely consistent with C3, but it is consistent with MM7 identified in the 1.3 mm continuum emission (Liu et al. 2017). MM7 was suggested to be at the early HMC stage (Liu et al. 2017). If the evolutionary sequence in this region is true, HC$_5$N seems to be enhanced in the HC H II region or HMC stages.

In general, the spatial distribution of HC$_3$N is more extended than that of HC$_5$N. This is caused by the fact that the upper-state energy of the HC$_3$N line ($E_{up}/k = 24.0$ K) is much lower than that of HC$_5$N, and could be excited in warm envelopes. The peak positions of the HC$_3$N emission are consistent with the continuum peaks, except for G16.57-0.05, where the HC$_3$N peak is slightly shifted in a southeastward direction from the continuum peak. The peak shift of molecular emission from the continuum emission is also seen in other COMs, and in a figure presented by Qin et al. (2022). Although we could not confirm the origin of the peak shifts with the current angular-resolution data, this source may consist of a binary system with a molecular-line-rich source and a line-poor source. In G9.62+0.19, the emission peak of HC$_3$N is almost consistent with C3, but the peak is also extended to MM7. From comparison of the features of HC$_5$N and HC$_3$N, HC$_5$N is more enhanced at Core C2, which is likely irradiated by the UV radiation from the central source in the HC H II region.

The spatial distributions of CCH are clearly different from the other molecules. The spatial distributions of CCH are extended. Holes can be seen at the continuum peaks in G9.62+0.19, G10.47+0.03, and G12.89+0.49. Such anticorrelations between CCH and continuum emission and cyanopolyynes support the prediction of chemical simulations (Taniguchi et al. 2019a) and the interpretation of single-dish observations

Table 5
Results of 2D Gaussian Fitting

| Core | Peak Position | | Size | Size[a] | PA | Peak Flux |
	R.A. (J2000)	Decl. (J2000)	($''$)	(pc)	(deg)	(mJy beam^{-1})
G9.62+0.19 C1	18^h 06^{m}14^{s}9297 (0^{s}0036)	−20°31′42″9012 (0″0303)	1.09 (0.22) × 1.01 (0.34)	0.027 (0.005) × 0.025 (0.009)	9.6 (72.6)	62.3 (3.1)
G9.62+0.19 C2	18^h 06^{m}14^{s}6557 (0^{s}0078)	−20°31′31″6473 (0″0621)	1.64 (0.41) × 1.24 (0.32)	0.041 (0.010) × 0.031 (0.008)	110 (80)	29.0 (2.7)
G9.62+0.19 C3	18^h 06^{m}14^{s}8640 (0^{s}0085)	−20°31′39″5432 (0″1168)	2.60 (0.50) × 1.93 (0.52)	0.066 (0.013) × 0.049 (0.013)	154 (37)	19.6 (2.0)
G10.47+0.03	18^h 08^{m}38^{s}2249 (0^{s}0007)	−19°51′50″3098 (0″0052)	1.14 (0.05) × 0.93 (0.03)	0.059 (0.003) × 0.048 (0.001)	117.3 (9.1)	588.2 (5.3)
G12.89+0.49	18^h 11^{m}51^{s}4509 (0^{s}0057)	−17°31′28″9450 (0″0552)	2.19 (0.29) × 1.84 (0.25)	0.032 (0.004) × 0.027 (0.004)	88 (81)	41.4 (2.6)
G16.57-0.05	18^h 21^{m}09^{s}0448 (0^{s}0029)	−14°31′47″9005 (0″0337)	2.51 (0.13) × 1.63 (0.08)	0.057 (0.003) × 0.037 (0.002)	125.8 (5.0)	22.35 (0.78)
G19.88-0.53 C1	18^h 29^{m}14^{s}3582 (0^{s}0023)	−11°50′22″5733 (0″0295)	2.74 (0.12) × 1.25 (0.06)	0.044 (0.002) × 0.020 (0.001)	132 (2)	17.79 (0.49)
G19.88-0.53 C2	18^h 29^{m}14^{s}4285 (0^{s}0023)	−11°50′24″0739 (0″0293)	2.08 (0.14) × 1.77(0.15)	0.033 (0.002) × 0.028 (0.002)	56 (22)	14.83 (0.48)

Notes. Numbers in parentheses indicate the fitting errors. The reported size and position angle are values deconvolved from the beam.
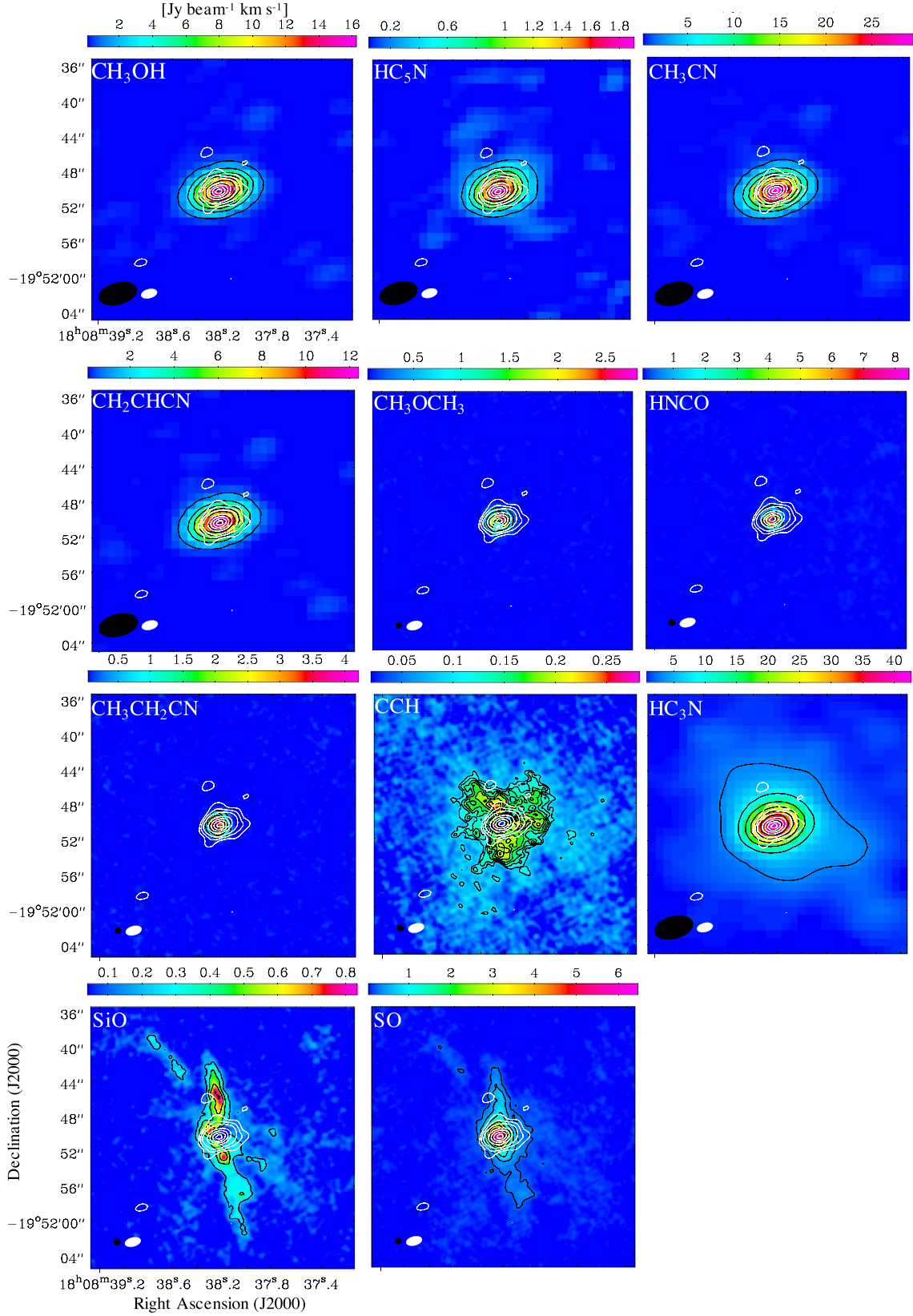[a] The source distances summarized in Table 1 are adopted.
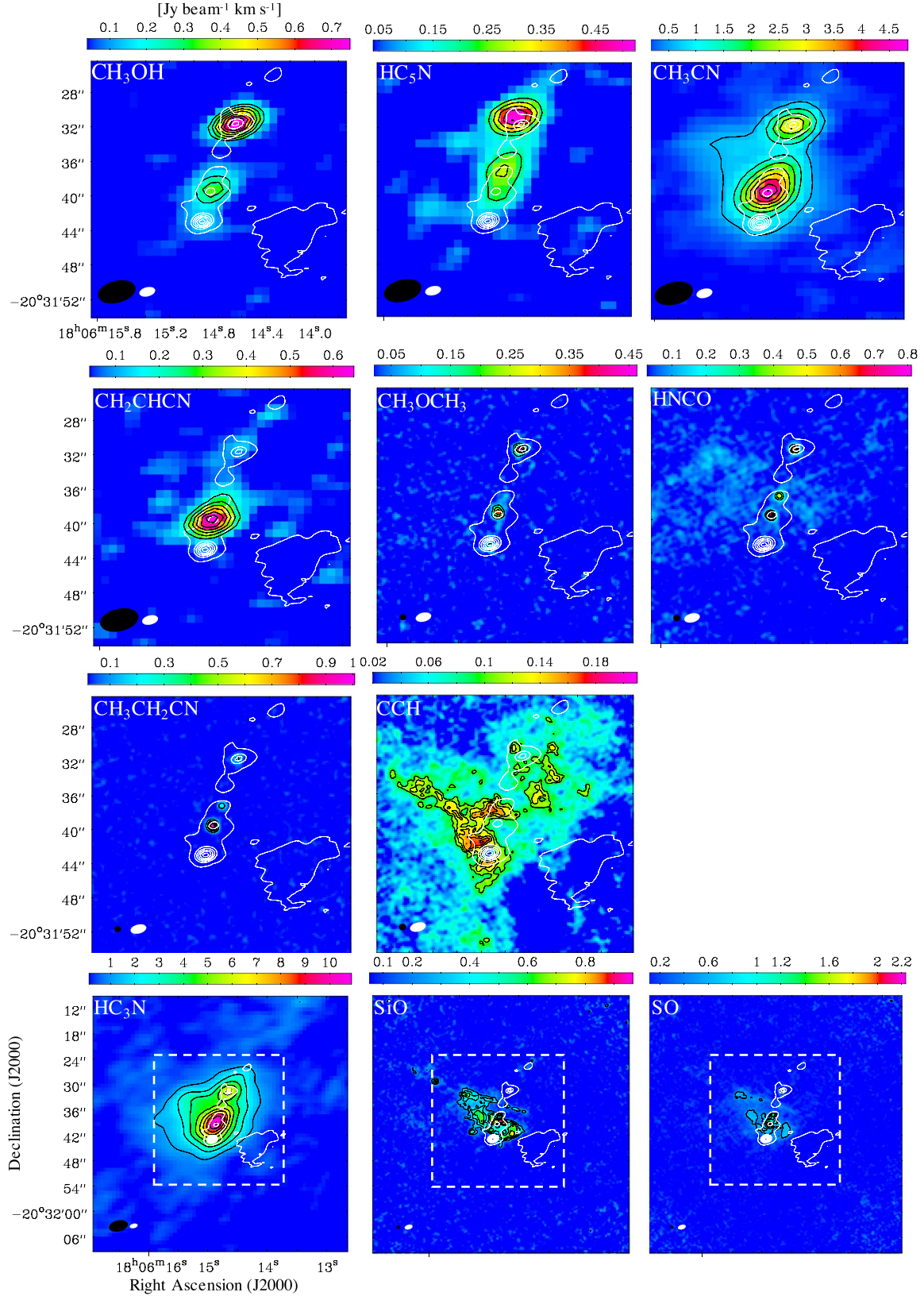
Figure 2. Moment 0 maps (combination of the 12 m and 7 m arrays) of molecular lines toward G9.62+0.19. The white contours indicate the continuum emission, which is the same as in Figure 1. The black and white ellipses at the bottom-left corner indicate the angular resolution for the moment 0 maps of molecular lines and the continuum emission, respectively. Information of angular resolution, noise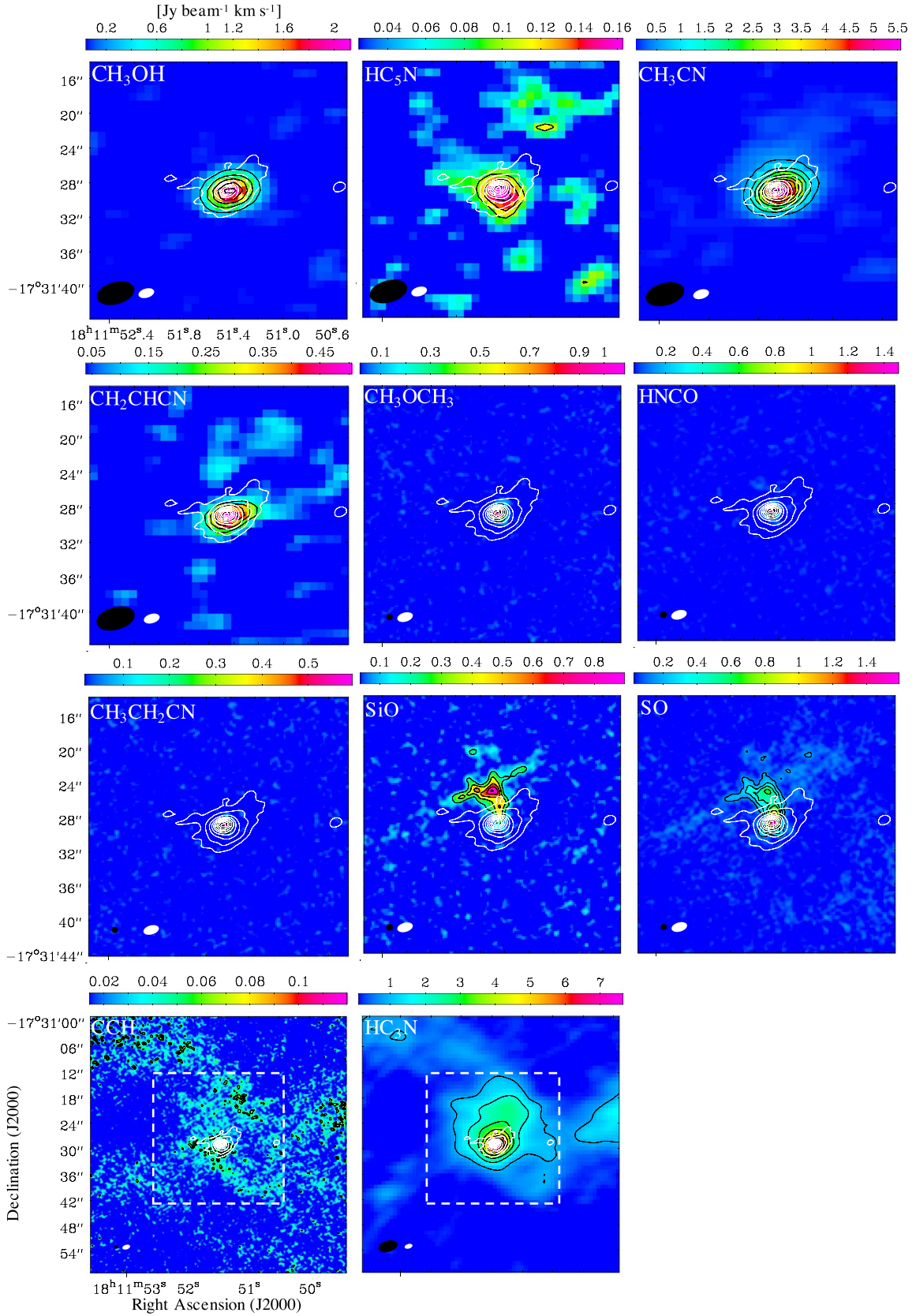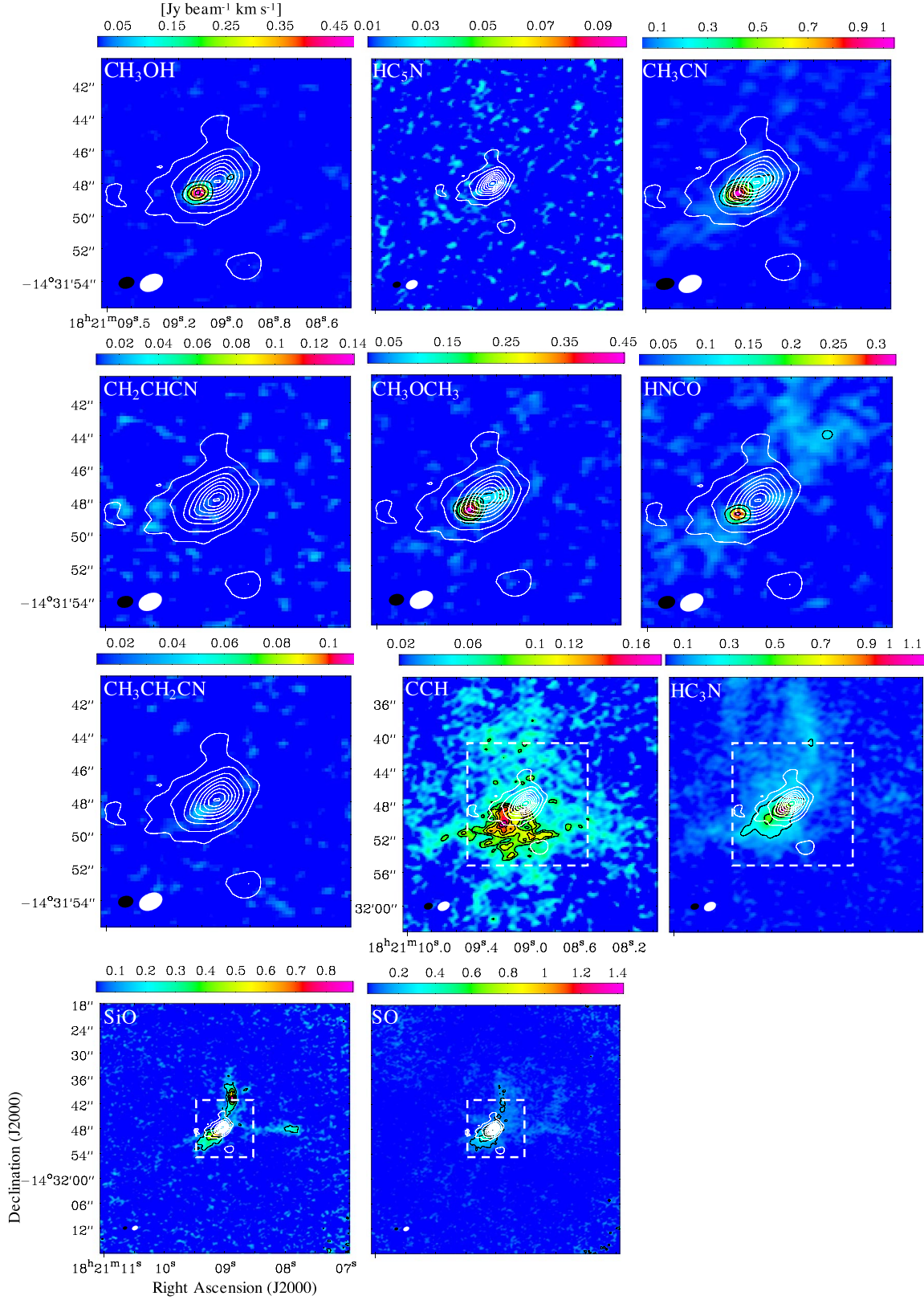 levels, and black contour levels are summarized in Table 6. The dashed squares in the panels of HC$_3$N, SiO, and SO indicate the region in the other panels.
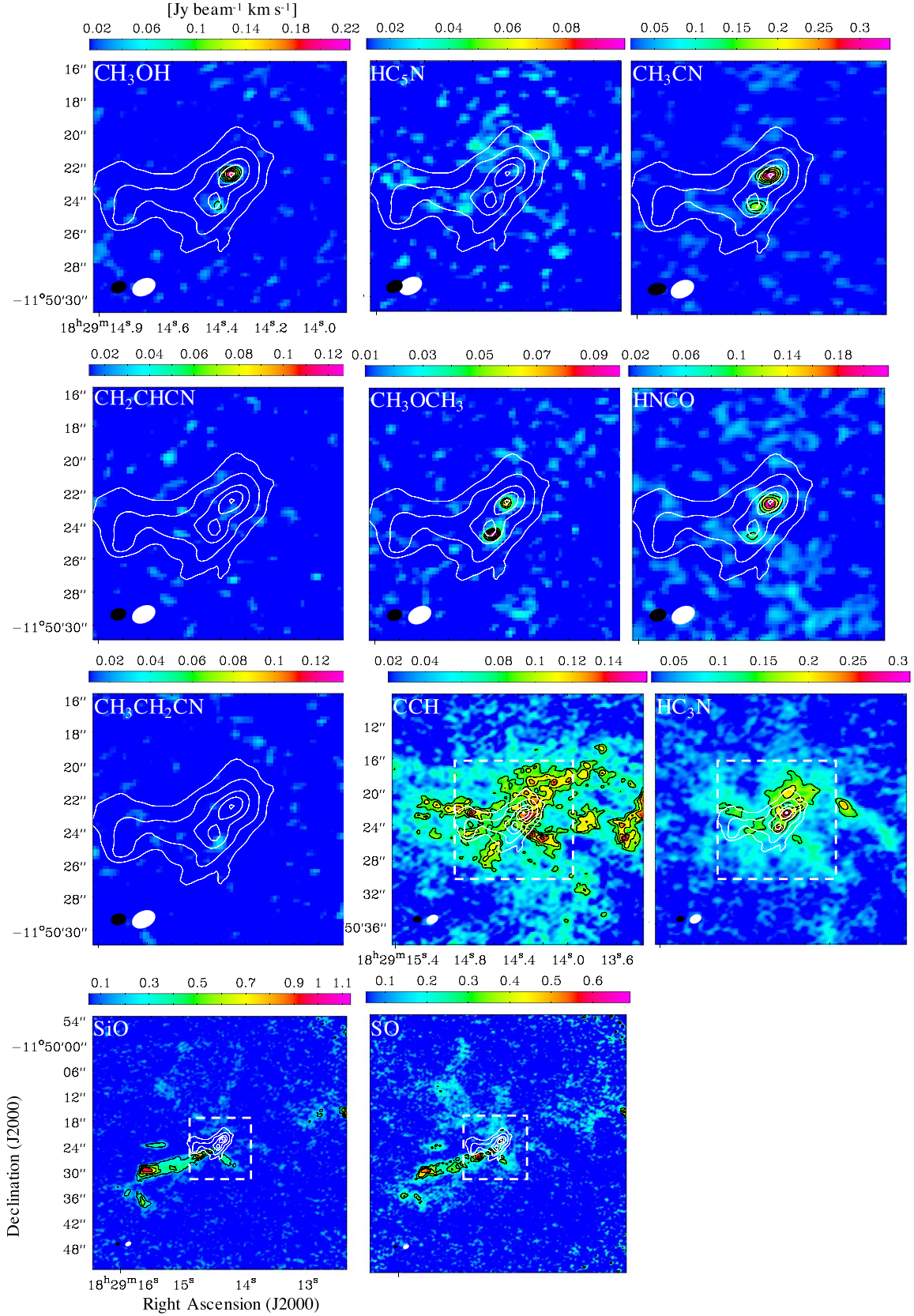
Figure 3. Moment 0 maps (combination of the 12 m and 7 m arrays) of molecular lines toward G10.47+0.03. The white contours indicate the continuum emission, which is the same as in Figure 1. The black and white ellipses at the bottom-left corner indicate the angular resolution for the moment 0 maps of molecular lines and the continuum emission, respectively. Information of angular resolution, noise levels, and black contour levels are summarized in Table 6.

Figure 4. Moment 0 maps (combination of the 12 m and 7 m arrays) of molecular lines toward G12.89+0.49. The white contours indicate the continuum emission, which is the same as in Figure 1. The black and white ellipses at the bottom-left corner indicate the angular resolution for the moment 0 maps of molecular lines and the continuum emission, respectively. Information of angular resolution, noise levels, and black contour levels are summarized in Table 6. The dashed squares in the panels of CCH and HC$_3$N indicate the region in the other panels.

Figure 5. Moment 0 maps (combination of the 12 m and 7 m arrays) of molecular lines toward G16.57-0.05. The white contours indicate the continuum emission, which is the same as in Figure 1. The black and white ellipses at the bottom-left corner indicate the angular resolution for the moment 0 maps of molecular lines and the continuum emission, respectively. Information of angular resolution, noise levels, and black contour levels are summarized in Table 6. The dashed squares in the panels of CCH, HC$_3$N, SiO, and SO indicate the region in the other panels.

Figure 6. Moment 0 maps (combination of the 12 m and 7 m arrays) of molecular lines toward G19.88-0.53. The white contours indicate the continuum emission, which is the same as in Figure 1. The black and white ellipses at the bottom-left corner indicate the angular resolution for the moment 0 maps of molecular lines and the continuum emission, respectively. Information of angular resolution, noise levels, and black contour levels are summarized in Table 6. The dashed squares in the panels of CCH, HC₃N, SiO, and SO indicate the region in the other panels.

Table 6
Information on the Moment 0 Maps

Molecule	G9.62+0.19			G10.47+0.03			G12.89+0.49			G16.57-0.05			G19.88-0.53		
	Ang. Res. (PA)	rms[a]	Contour Levels	Ang. Res. (PA)	rms[a]	Contour Levels	Ang. Res. (PA)	rms[a]	Contour Levels	Ang. Res. (PA)	rms[a]	Contour Levels	Ang. Res. (PA)	rms[a]	Contour Levels
CH_3OH	4".5 × 2".5 (−75°.7)	0.04	5–17σ (2σ step)	4".5 × 2".5 (−74°.8)	0.1	10–150σ (20σ step)	4".4 × 2".5 (−74°.5)	0.04	10–50σ (10σ step)	0".97 × 0".71 (−76°.3)	0.013	5–35σ (10σ step)	0".97 × 0".71 (−75°.1)	0.014	4–12σ (2σ step)
HC_5N	4".5 × 2".5 (−75°.7)	0.04	5–13σ (2σ step)	4".5 × 2".5 (−74°.8)	0.05	5–35σ (5σ step)	4".4 × 2".5 (−74°.5)	0.025	4, 5, 6σ	0".97 × 0".71 (−76°.3)	0.01	···	0".97 × 0".71 (−75°.1)	0.012	···
CH_3CN	4".5 × 2".6 (−76°.4)	0.06	10–80σ (10σ step)	4".6 × 2".6 (−75°.2)	0.2	10–130σ (20σ step)	4".5 × 2".6 (−74°.7)	0.06	10–90σ (10σ step)	1".1 × 0".71 (−80°.1)	0.015	10–60σ (10σ step)	1".1 × 0".72 (−79°.6)	0.017	5–17σ (3σ step)
CH_2CHCN	4".5 × 2".6 (−76°.7)	0.04	5–15σ (2σ step)	4".6 × 2".6 (−75°.4)	0.09	10–130σ (20σ step)	4".5 × 2".6 (−74°.8)	0.04	5–11σ (2σ step)	0".99 × 0".71 (−78°.5)	0.008	···	0".97 × 0".72 (−77°.2)	0.013	···
CH_3OCH_3	0".74 × 0".70 (82°.9)	0.02	5–20σ (5σ step)	0".74 × 0".70 (81°.3)	0.03	10–90σ (20σ step)	0".73 × 0".70 (83°.0)	0.017	10–60σ (10σ step)	0".92 × 0".70 (−79°.9)	0.014	5, 8, 10, 15, 20, 25, 30σ	0".91 × 0".68 (−77°.4)	0.010	5–10σ
HNCO	0".81 × 0".76 (84°.8)	0.025	10–30σ (5σ step)	0".81 × 0".76 (84°.1)	0.04	10, 50–200σ (50σ step)	0".80 × 0".76 (84°.0)	0.025	10–50σ (10σ step)	1".0 × 0".76 (−76°.9)	0.02	5, 10, 15σ	1".0 × 0".76 (−75°.5)	0.015	5–14σ (3σ step)
CH_3CH_2CN	0".74 × 0".70 (83°.4)	0.017	10–50σ (10σ step)	0".74 × 0".71 (81°.1)	0.041	10, 30, 50, 70, 90, 100σ	0".73 × 0".70 (81°.3)	0.017	5–30σ (5σ step)	0".93 × 0".70 (−79°.8)	0.011	···	0".92 × 0".70 (−78°.3)	0.009	···
CCH	0".82 × 0".76 (87°.1)	0.02	5–9σ	0".82 × 0".77 (87°.5)	0.02	5–12σ	0".81 × 0".76 (87°.8)	0.014	4–7σ	1".0 × 0".76 (−76°.6)	0.019	4–9σ	1".0 × 0".76 (−75°.1)	0.02	4–7σ
HC_3N	4".5 × 2".6 (−76°.2)	0.12	10–90σ (10σ step)	4".6 × 2".6 (−75°.1)	0.3	10–130σ (20σ step)	4".6 × 2".6 (−74°.1)	0.09	10–80σ (10σ step)	1".0 × 0".72 (−77°.7)	0.023	10–50σ (10σ step)	1".0 × 0".73 (−76°.9)	0.025	5, 7, 9, 11σ
SiO	0".81 × 0".76 (87°.8)	0.05	5–17σ (3σ step)	0".81 × 0".76 (87°.3)	0.04	5–20σ (5σ step)	0".80 × 0".76 (87°.2)	0.035	5–25σ (5σ step)	1".0 × 0".76 (−76°.8)	0.036	5–20σ (5σ step)	1".0 × 0".76 (−75°.7)	0.05	5–17σ (4σ step)
SO	0".74 × 0".70 (82°.6)	0.05	10, 15, 20, 30, 40σ	0".74 × 0".70 (82°.2)	0.05	5, 10, 20–120σ (20σ step)	0".73 × 0".70 (83°.4)	0.03	5, 10, 15, 20–50σ (10σ step)	0".92 × 0".70 (−79°.9)	0.03	5, 10, 15, 20, 30, 40σ	0".90 × 0".68 (−77°.4)	0.054	5, 7, 9, 11σ

Note.
[a] Unit is Jy beam^{-1} km s^{-1}.

(Taniguchi et al. 2021a; see discussion in Section 4.1). Around Core C2 of G9.62+0.19, the CCH emission is very fragmented. This may be caused by the cold envelopes being blown away by the stellar feedback in Core C2.

The CH_3OH, CH_3OCH_3, and HNCO lines have been detected in all of the sources, and the peaks of their spatial distributions are consistent with the continuum cores except for G16.57-0.05. The molecular peaks in G16.57-0.05 are consistent with each other and shifted in a southeastward direction from the continuum peak as well as the HC_3N line. In G9.62+0.19, an HNCO peak is located between Cores C2 and C3, and not coincident with the continuum peak. This HNCO peak is consistent with a dense hot core, MM7, associated with molecular outflows identified in Liu et al. (2017).

The CH_3CN line has been detected in all of the target sources. As in the case of other molecular lines in G16.57-0.05, the peak position of CH_3CN is located at the southeast position from the continuum core.

In G9.62+0.19, the N-bearing COMs show stronger peak fluxes at C3 compared to C2. This trend is opposite to CH_3OH, CH_3OCH_3, and HC_5N, but similar to HNCO and HC_3N. This may mean that these N-bearing COMs prefer the younger HMC stages rather than the evolved HC H II region stage. In the CH_3CH_2CN moment 0 map toward G9.62+0.19, a peak is located between Cores C2 and C3, and this peak is coincident with the HNCO peak, or MM7 (Liu et al. 2017).

3.3. Spectral Analyses

Under the assumption of LTE, we derived the physical conditions using the CH_3CN $J = 5-4$ K-ladder ($K = 0-4$) emission ($E_{up}/k = $ 13.2, 20.4, 41.8, 77.5, and 127.5 K for $K = 0$, 1, 2, 3, and 4, respectively). The upper-energy levels, Einstein coefficients, degeneracies, and partition functions are from the CDMS database (Endres et al. 2016). Details about the formalism for the CASSIS software are provided by a document.[16] We measured the rms noise levels of the spectra, and these noise levels were taken into consideration in the spectral fitting. The coordinates of each core are summarized in Table 5.

Figure 7 shows the spectra of CH_3CN at each core. Its K-ladder lines have been detected from all of the cores. The column density (N), excitation temperature (T_{ex}), line width (FWHM), systemic velocity (V_{LSR}), and size were treated as free parameters in the Markov Chain Monte Carlo (MCMC) method for the CH_3CN lines. Table 7 summarizes the results of the MCMC analysis. Red curves in Figure 7 indicate the best-fit models. We applied two-component fitting for the spectra at G9.62+0.19 C3, G10.47+0.03, and G12.89+0.49, because the one-component fitting could not reproduce the observed spectra. The wing emission can be seen, especially in the $K = 4$ line. This wing emission is likely to originate from molecular outflows, because the outflow tracers such as the SiO and SO lines have been detected in all of the sources (Section 3.2). We then excluded the $K = 4$ line from the fitting in the MCMC analysis due to non-Gaussian line profiles. Table 9 in Appendix A summarizes the optical depth of each line. For sources containing line emission with different optical depths, the column densities and source sizes can be constrained reasonably. For those with only optically thin line emission, the column densities and source sizes are degenerate. However, the

---

[16] http://cassis.irap.omp.eu/docs/RadiativeTransfer.pdf

derived excitation temperature, line width, and velocity are not (or are less) affected by this. To compare the abundance ratios with the other molecules, if the source size is fixed, this will not significantly affect the results.

Figures 8–11 show spectra of HC_5N, O-bearing COMs (CH_3OH and CH_3OCH_3), HNCO, and N-bearing COMs (CH_2CHCN and CH_3CH_2CN) at each core, respectively. The HC_5N ($J = 35-34$) line has been detected from four cores: G9.62+0.19 C2, G9.62+0.19 C3, G10.47+0.03, and G12.89 +0.49 (Figure 8). The CH_3OH line has been detected with sufficient signal-to-noise ratio from all of the cores except for G19.88-0.53 C2, in which the line seems to be tentatively detected (Figure 9). We could not fit the CH_3OH line at G19.88-0.53 C2. We note that the upper-state energy of the observed CH_3OH line (302.9 K) is high. This may cause the nondetection of the CH_3OH line in G19.88-0.53 C2, and its nondetection does not mean that CH_3OH is deficient.

The CH_3OCH_3 line has been detected from all of the cores. The CH_3OCH_3 spectrum in G10.47+0.03 shows a clear double-peaked feature. As seen in its moment 0 map (Figure 3), its spatial distribution is a ring-like structure. The dust optical thickness at Band 3 is derived to be ~0.07–0.16, with an assumption of $T_{dust} = 100-200$ K. Thus, the dust emission is optically thin at this frequency band. In addition, the brightness temperature of the continuum emission is around 18 K, which is much lower than the excitation temperatures of molecular lines (~137–195 K; Table 7). Hence, we concluded that such a ring-like feature is not caused by the absorption against the continuum emission. We constructed channel maps of the CH_3OCH_3 line toward this source, as shown in Figure 16 in Appendix B to investigate the origin of this unique structure. A rotating and expanding shell motion plus skewed emission distribution toward the northwest could reproduce the observed velocity structure. We will discuss detailed analyses of the kinematics of this line in a future paper.

The HNCO line has been detected from all of the cores except for G9.62+0.19 C1 (Figure 10). The N-bearing COMs have been detected from the four cores (G9.62+0.19 C2, G9.62 +0.19 C3, G10.47+0.03, and G12.89+0.49), as shown in Figure 11, and these four cores match ones where the HC_5N line has been detected (Figure 8). The absorption feature at the blueshifted side in the CH_3CH_2CN spectrum in G10.47+0.03 may indicate an expansion motion of gas.

We conducted the spectral analyses of these molecular lines (Figures 8–11) by the MCMC method in CASSIS. Since we have clearly identified only one line or a few blended lines for these molecules, we treated their column density, FWHM, and V_{LSR} as free parameters, and fixed the excitation temperature and size. The excitation temperatures were fixed at the values derived from the CH_3CN analysis: 86.4 K (G9.62+0.19 C1), 150 K (G9.62+0.19 C2), 113 K (G9.62+0.19 C3), 194.8 K (G10.47+0.03, component 1), 137.3 K (G10.47+0.03, component 2), 100 K (G12.89+0.49), 135 K (G16.57-0.05), 205 K (G19.88-0.53 C1), and 88 K (G19.88-0.53 C2), respectively. The size values were fixed at the sizes of the beam: 1″01 (G9.62+0.19 C1), 1″24 (G9.62+0.19 C2), 1″93 (G9.62+0.19 C3), 0″93 (G10.47+0.03), 1″84 (G12.89+0.49), 1″63 (G16.57-0.05), 1″25 (G19.88-0.53 C1), and 1″77 (G19.88-0.53 C2), respectively. This means that the derived column densities are the beam-averaged values. The rms noise levels were considered in the spectral fitting. Red curves in Figures 8–11 indicate the best-fit models. Table 8 summarizes
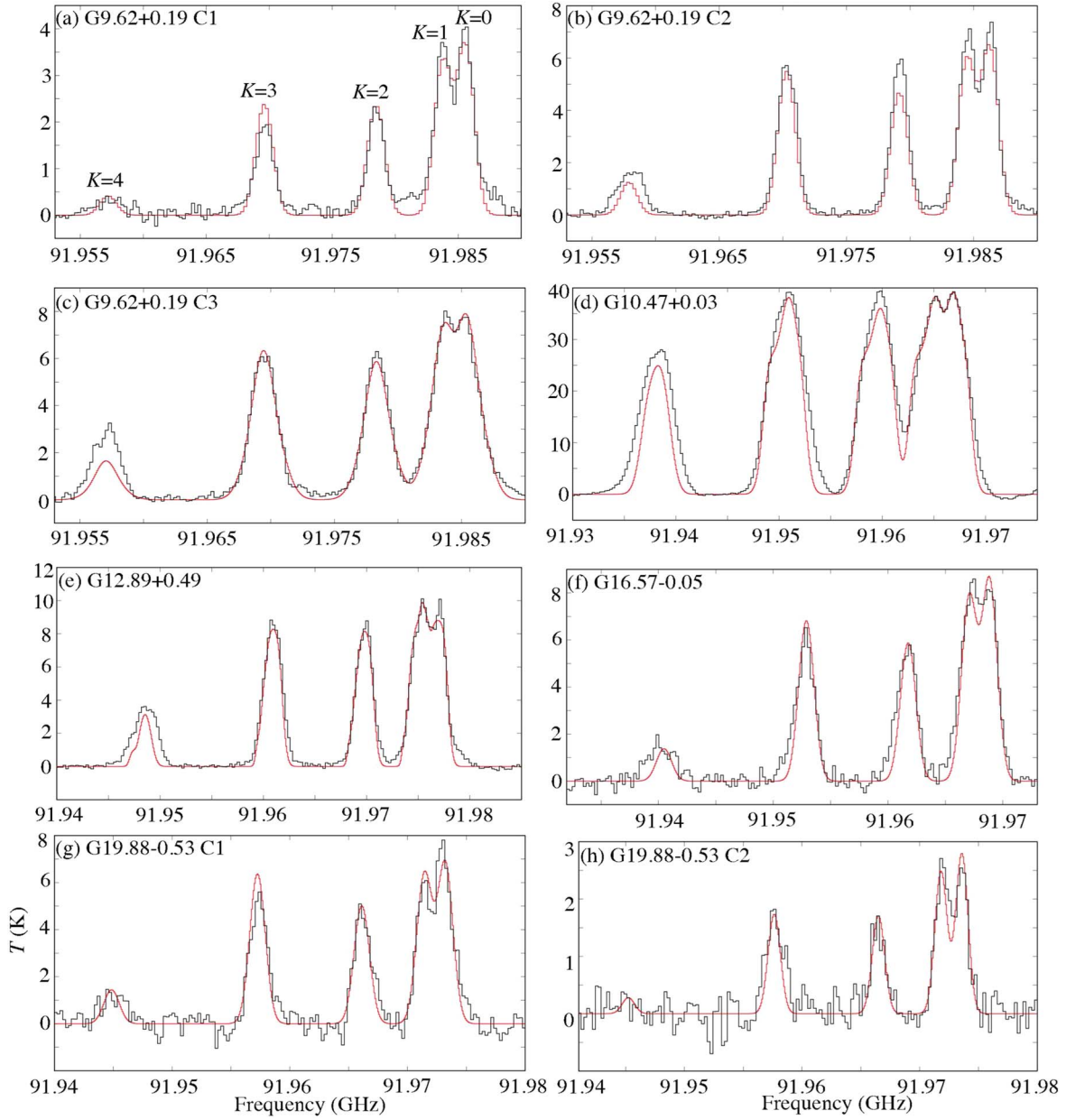
Figure 7. Spectra of the CH$_3$CN lines ($J = 5_K–4_K$, $K = 0–4$) at each core. The red curves show the best-fit results in the CASSIS software.

Table 7
Results of MCMC Analysis of CH$_3$CN

Core	N (cm^{-2})	T_{ex} (K)	FWHM (km s^{-1})	V_{LSR} (km s^{-1})	Size ($''$)
G9.62+0.19 C1	$(2.8 \pm 0.6) \times 10^{15}$	86.40 ± 0.18	5.04 ± 0.01	4.9 ± 0.3	1.488 ± 0.014
G9.62+0.19 C2	$(1.36 \pm 0.04) \times 10^{16}$	150.02 ± 0.01	5.003 ± 0.001	3.2 ± 0.4	1.497 ± 0.005
G9.62+0.19 C3 (component 1)	$(8.304 \pm 0.006) \times 10^{15}$	119.84 ± 0.14	5.14 ± 0.03	5.504 ± 0.004	1.316 ± 0.005
G9.62+0.19 C3 (component 2)	$(7.00 \pm 0.01) \times 10^{16}$	112.6 ± 0.3	8.49 ± 0.01	5.214 ± 0.008	0.735 ± 0.002
G10.47+0.03 (component 1)	$(2.27 \pm 0.03) \times 10^{16}$	194.80 ± 0.03	4.69 ± 0.02	65.792 ± 0.007	2.085 ± 0.013
G10.47+0.03 (component 2)	$(4.982 \pm 0.001) \times 10^{17}$	137.33 ± 0.03	6.84 ± 0.01	67.09 ± 0.06	1.878 ± 0.009
G12.89+0.49 (component 1)	$(2.98 \pm 0.03) \times 10^{16}$	102.84 ± 0.07	1.87 ± 0.03	37.22 ± 0.05	0.444 ± 0.007
G12.89+0.49 (component 2)	$(4.3 \pm 0.4) \times 10^{16}$	100.15 ± 0.19	4.06 ± 0.10	33.145 ± 0.008	1.195 ± 0.013
G16.57-0.05	$(3.6 \pm 0.3) \times 10^{15}$	134.98 ± 0.05	4.99 ± 0.05	59.45 ± 0.02	1.16 ± 0.11
G19.88-0.53 C1	$(6.26 \pm 0.18) \times 10^{15}$	205.020 ± 0.004	4.94 ± 0.03	45.22 ± 0.02	1.02 ± 0.03
G19.88-0.53 C2	$(2.96 \pm 0.19) \times 10^{14}$	88.06 ± 0.02	3.5 ± 0.3	43.94 ± 0.04	2.5 ± 0.3

Note. The errors indicate the standard deviation derived from the MCMC analysis.
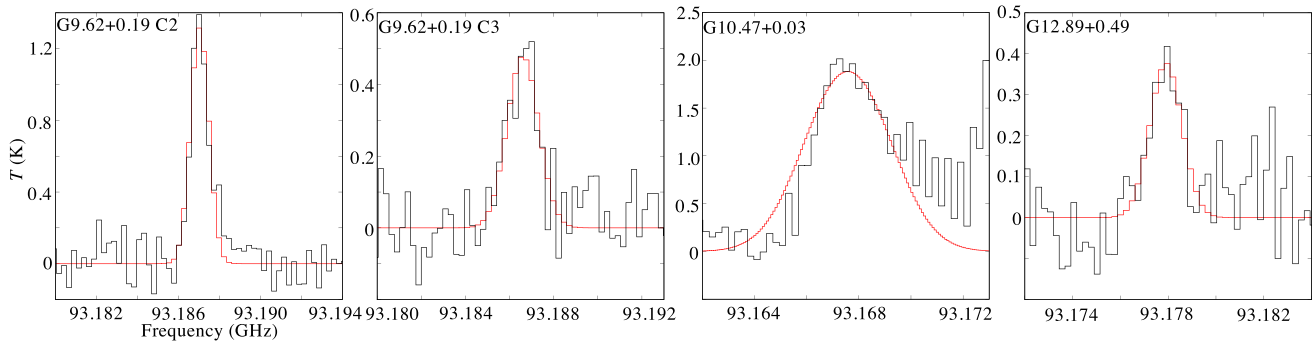
Figure 8. Spectra of the HC$_5$N ($J = 35-34$) line at each core. The red curves show the best-fit results in the CASSIS software.

the column density, line width, and velocity component derived by the MCMC method. All of these lines, except for CH$_3$OH in G10.47+0.03, are optically thin ($\tau < 0.3$). The optical thickness of the CH$_3$OH line in G10.47+0.03 is 2.09.

4. Discussions

In the MCMC analyses (Section 3.3), we took the rms noise levels of the spectra into consideration, but uncertainties brought by other factors, such as the absolute calibration uncertainties, are not included. The typical absolute calibration uncertainty is 5% at Band 3. Besides, there are other possible uncertainties, such as molecular emission size and beam size. Taking these factors into consideration, we added 10% errors to the errors of each column density derived by the MCMC methods in the following sections.

4.1. Comparisons of Spatial Distributions and Line Features

We compare spatial distributions among O-bearing COMs, N-bearing COMs, and HC$_5$N at each core. In these comparisons, as we have already mentioned in Section 3.2, we selected molecular pairs which were observed simultaneously: CH$_3$OH versus CH$_3$CN, CH$_3$OH versus HC$_5$N, and CH$_3$OCH$_3$ versus CH$_3$CH$_2$CN. Each pair has the same ang. res. In the case of G16.57-0.05 and G19.88-0.53, we only show comparisons between CH$_3$OH and CH$_3$CN, because the other molecules were not detected.

Figure 12 shows comparisons of the spatial distributions between each pair toward the five sources. In G9.62+0.19, the peak positions of CH$_3$OH and CH$_3$CN are well coincident with each other. On the other hand, the peak positions between CH$_3$OH and HC$_5$N, and CH$_3$OCH$_3$ and CH$_3$CH$_2$CN may be slightly shifted, but the differences are within the beam sizes. There are no contours of CH$_3$CH$_2$CN at the C2 position, because the relative intensity of its peak at C2 is much weaker than that at C3.

The peak positions of CH$_3$OH, CH$_3$CN, and HC$_5$N are well consistent with each other in G10.47+0.03 and G12.89+0.49, and their peaks are associated with the continuum cores. The peaks of CH$_3$OCH$_3$ and CH$_3$CH$_2$CN are located at the west and east, respectively, in G10.47+0.03, whereas their peaks are well consistent with the continuum peak in G12.89+0.49.

Here, we simulated the line intensity of the CH$_3$OH line in the CASSIS software, using the results of our chemical simulations. Details about our chemical simulations are described in Section 4.3. We assume that the CH$_3$OH emission does not come from the hot-core regions, thermal sublimation does not occur, and the excitation temperature should be below 100 K. In our

chemical simulations, the maximum abundance of CH$_3$OH with respect to total hydrogen nuclei before its thermal sublimation is around 5×10^{-9}. We further assume that the H$_2$ column density is 10^{24} cm^{-2} and the CH$_3$OH excitation temperature is 90 K, which is the corresponding temperature at the maximum CH$_3$OH abundance. With these conditions, the observed CH$_3$OH line is not excited and should not have been detected. Therefore, the observed CH$_3$OH line should trace the hot-core regions with temperatures above $\sim$100 K in which thermal sublimation of CH$_3$OH occurs.

Both the CH$_3$OH and HC$_5$N lines are optically thin, except for CH$_3$OH in G10.47+0.03. In addition, the CH$_3$OH and HC$_5$N emissions show single peaks toward the source positions and the emissions are almost unresolved, where the beam sizes of both observations are almost identical. Thus, both the CH$_3$OH and HC$_5$N emission trace the hot and dense gas regions associated with the HMPOs.

These results support previous results and implications from chemical simulations (Taniguchi et al. 2019a) and single-dish telescope observations (Taniguchi et al. 2021a): cyanopolyynes around MYSOs exist in higher temperature regions ($\geqslant$85 K) than regions where WCCC occurs ($\sim$25–30 K). This means that cyanopolyynes can survive in hot regions where radical-type carbon-chain species (e.g., CCH and CCS) are efficiently destroyed by the gas-phase reactions with O and H$_2$ (Taniguchi et al. 2019a). The moment 0 maps (Figures 2–4) support this picture. The CCH emission is systematically different from that of CH$_3$OH and HC$_5$N: it has rather extended, clumpy features, and is deficient at the continuum peaks. In other words, the carbon-chain chemistry around MYSOs is not WCCC occurring around low-mass YSOs, but another mechanism in hot-core regions ($>$100 K). We call this carbon-chain chemistry occurring in hot-core regions around MYSOs *hot carbon-chain chemistry (HCCC)*.

Figure 13 shows a schematic view of WCCC and HCCC to distinguish them clearly. The WCCC mechanism indicates the formation processes of carbon-chain species, starting from CH$_4$ at temperatures around 25 K, corresponding to the sublimation temperature of CH$_4$. The HCCC mechanism represents not only gas-phase formation of cyanopolyynes around 25 K but also successive phenomena. In the HCCC mechanism, cyanopolyynes are formed in the warm gas by neutral–neutral reactions between C$_{2n}$H$_2$ and CN, adsorbed onto dust grains, and accumulated in ice mantles during the warm-up stage ($25 \leqslant T \leqslant 100$ K; Taniguchi et al. 2019a). After the temperature reaches 100 K, cyanopolyynes sublimate into the gas phase and show peak abundances, whereas the radical-type carbon-chain species (e.g., CCH) are depleted due to efficient destruction in
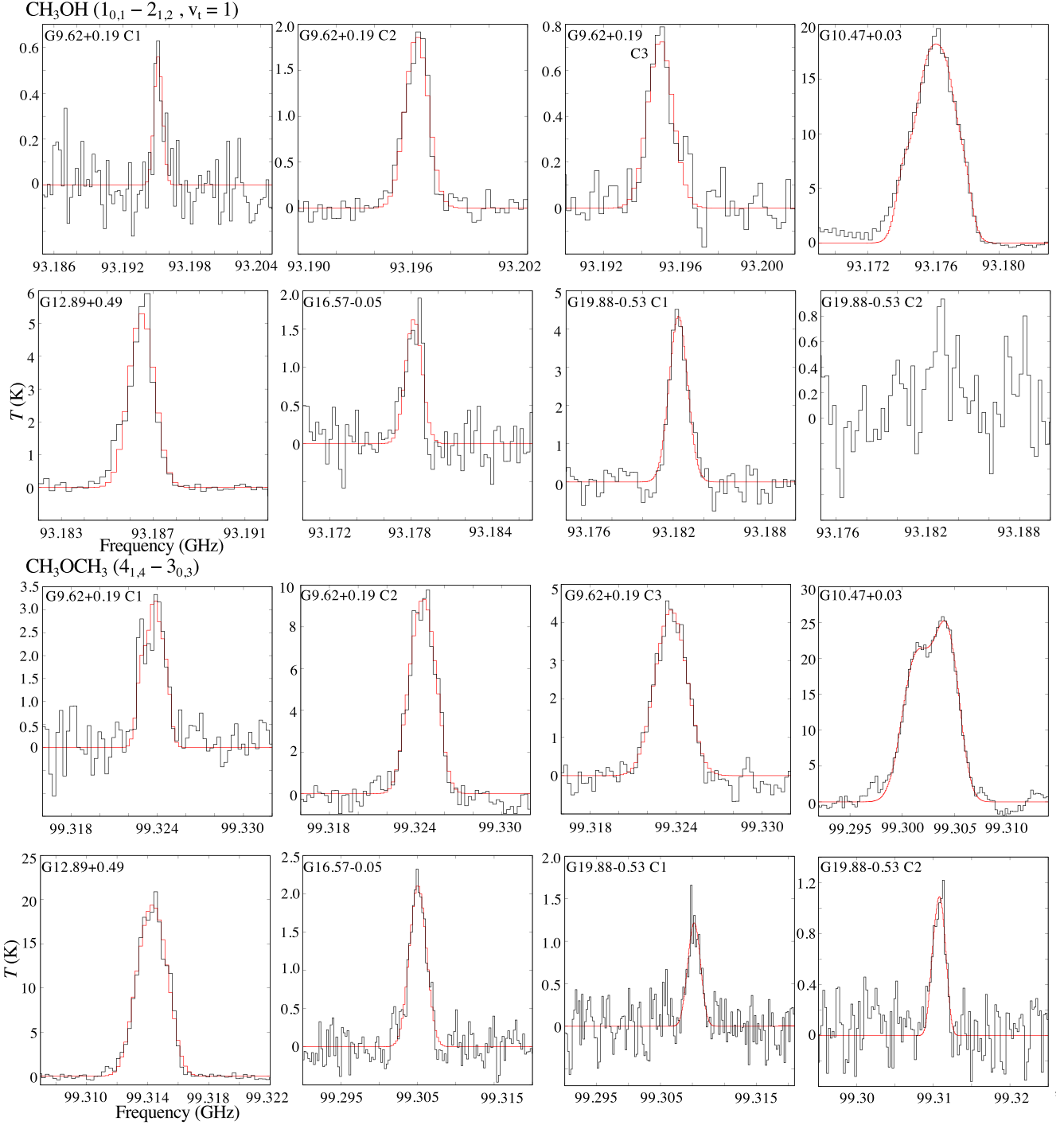
CH$_3$OH ($1_{0,1} - 2_{1,2}$, $v_t = 1$)

Figure 9. Spectra of the CH$_3$OH ($1_{1,0}-2_{1,2}$, $v_t = 1$) and CH$_3$OCH$_3$ ($4_{1,4}-3_{0,3}$) lines at each core. The red curves show the best-fit results in the CASSIS software.

the gas phase (Taniguchi et al. 2019a). We further discuss comparisons with our latest chemical simulations in Section 4.3.

In G16.57-0.05, the peak positions of CH$_3$OH and CH$_3$CN are well consistent with each other, but they are not coincident with the continuum core. Since the continuum flux in G16.57-0.05 is not higher than the other sources, the spatial difference between the continuum peak and the molecular emission appears to be real. In G19.88-0.53, the peak positions of CH$_3$OH and CH$_3$CN are well coincident each other, and they are associated with the continuum cores.

In summary, we cannot recognize clear chemical differentiation around the five MYSOs with the current ang. res. In G10.47 +0.03, the spatial distributions of CH$_3$OCH$_3$ and CH$_3$CH$_2$CN show different features. As mentioned in Section 3.3, the CH$_3$OCH$_3$ line in this source likely traces the expanding shell or an accretion disk. However, the CH$_3$CH$_2$CN line does not show such a double-peaked feature (Figure 11). Thus, their spatial distributions probably differ. Future higher-angular-resolution data are necessary to confirm the possible chemical differentiation.
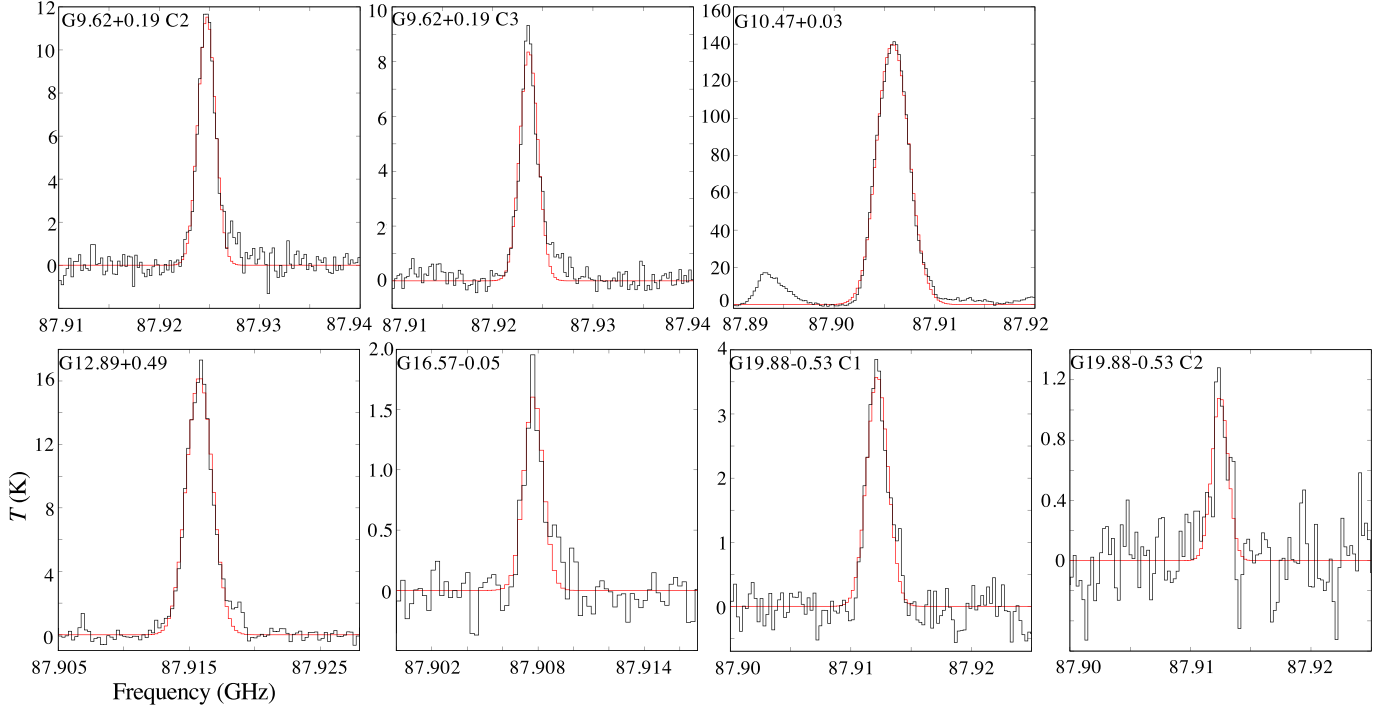
Figure 10. Spectra of the HNCO $(4_{0,4}-3_{0,3})$ line at each core. The red curves show the best-fit results in the CASSIS software.
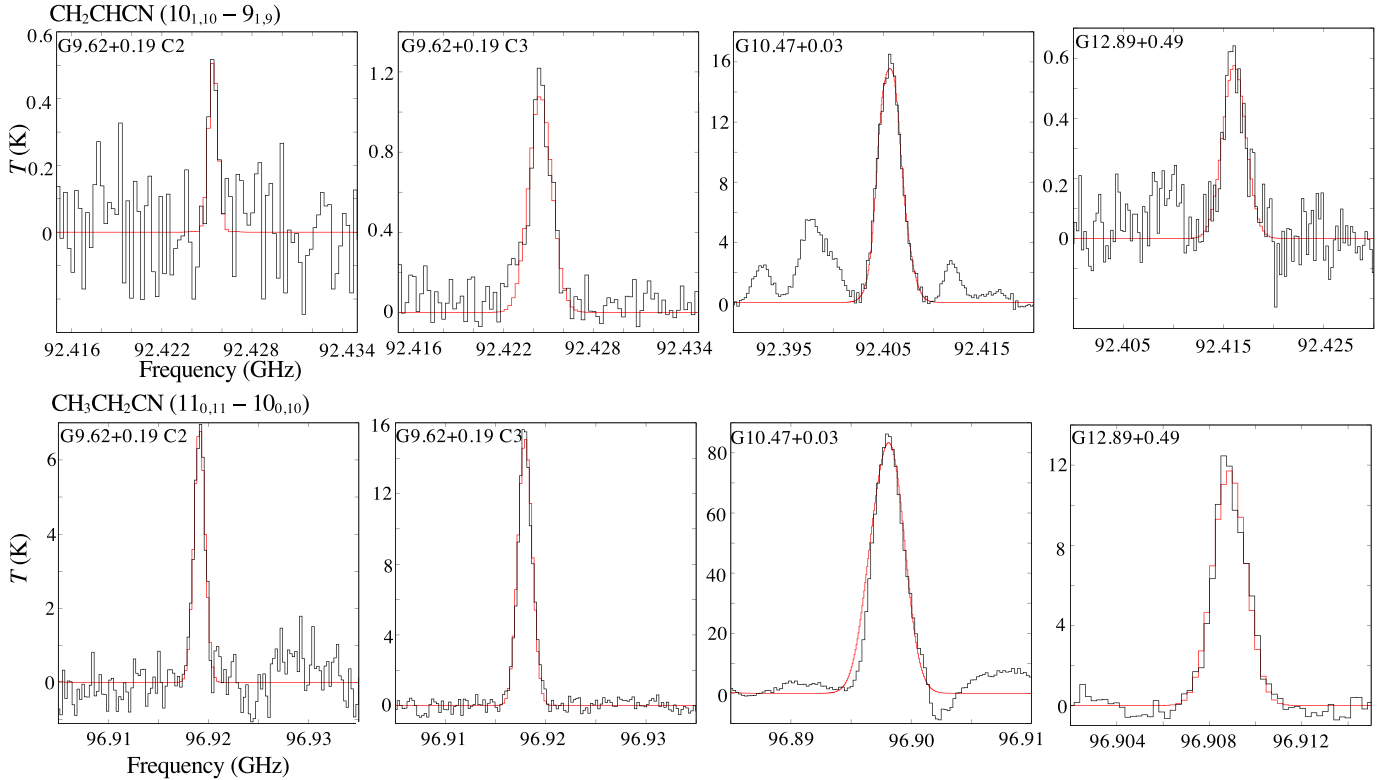
Figure 11. Spectra of the CH$_2$CHCN $(10_{1,10}-9_{1,9})$ and CH$_3$CH$_2$CN $(11_{0,11}-10_{0,10})$ lines at each core. The red curves show the best-fit results in the CASSIS software.

4.2. Comparison of Molecular Composition

The emission of HC$_5$N and COMs show point-like distributions. Although these data sets are inhomogeneous, it is still meaningful to compare the chemical composition among the different sources using the observed molecules. We derive molecular abundances with respect to CH$_3$CN ($=N(X)/N$ (CH$_3$CN), where X denotes molecular species) and compare them among each core. We used CH$_3$CN as a reference, because we consider that the spectral analysis of this species is most reliable due to its K-ladder lines (Section 3.3). We added

Table 8
Results of MCMC Analysis

Core	HC$_5$N			CH$_3$OH		
	N (cm^{-2})	FWHM (km s^{-1})	V_{LSR} (km s^{-1})	N (cm^{-2})	FWHM (km s^{-1})	V_{LSR} (km s^{-1})
G9.62+0.19 C1	⋯	⋯	⋯	$(1.01 \pm 0.05) \times 10^{18}$	2.56 ± 0.17	5.13 ± 0.06
G9.62+0.19 C2	$(5.37 \pm 0.07) \times 10^{14}$	3.38 ± 0.04	3.49 ± 0.02	$(2.33 \pm 0.02) \times 10^{18}$	4.50 ± 0.05	1.49 ± 0.02
G9.62+0.19 C3	$(1.27 \pm 0.03) \times 10^{14}$	5.31 ± 0.11	4.87 ± 0.07	$(5.4 \pm 0.1) \times 10^{17}$	5.10 ± 0.12	5.49 ± 0.05
G10.47+0.03 (component 1)	$(4.82 \pm 0.02) \times 10^{15}$[a]	11.997 ± 0.002	66.1000 ± 0.0003	$(5.517 \pm 0.007) \times 10^{19}$	5.09 ± 0.02	65.97 ± 0.01
G10.47+0.03 (component 2)	Fitted by single component			$(6.2 \pm 0.5) \times 10^{20}$	6.4 ± 0.2	66.5 ± 0.1
G12.89+0.49	$(1.01 \pm 0.05) \times 10^{14}$	5.23 ± 0.15	32.88 ± 0.13	$(4.53 \pm 0.02) \times 10^{18}$	4.07 ± 0.02	32.73 ± 0.01
G16.57-0.05	⋯	⋯	⋯	$(2.86 \pm 0.03) \times 10^{17}$	4.65 ± 0.05	59.36 ± 0.02
G19.88-0.53 C1	⋯	⋯	⋯	$(8.95 \pm 0.03) \times 10^{17}$	4.53 ± 0.02	46.10 ± 0.01
G19.88-0.53 C2	⋯	⋯	⋯	⋯	⋯	⋯

Core	CH$_3$OCH$_3$			HNCO		
	N (cm^{-2})	FWHM (km s^{-1})	V_{LSR} (km s^{-1})	N (cm^{-2})	FWHM (km s^{-1})	V_{LSR} (km s^{-1})
G9.62+0.19 C1	$(3.140 \pm 0.006) \times 10^{16}$	2.51 ± 0.01	4.507 ± 0.006	⋯	⋯	⋯
G9.62+0.19 C2	$(2.216 \pm 0.002) \times 10^{17}$	4.57 ± 0.01	2.228 ± 0.003	$(2.367 \pm 0.001) \times 10^{16}$	6.777 ± 0.004	1.778 ± 0.002
G9.62+0.19 C3	$(6.90 \pm 0.01) \times 10^{16}$	6.42 ± 0.01	4.775 ± 0.006	$(9.885 \pm 0.007) \times 10^{15}$	7.102 ± 0.006	5.545 ± 0.002
G10.47+0.03 (component 1)	$(1.263 \pm 0.004) \times 10^{18}$	6.76 ± 0.05	63.10 ± 0.09	$(4.7 \pm 0.6) \times 10^{17}$	8.3 ± 0.3	66.2 ± 0.1
G10.47+0.03 (component 2)	$(7.9 \pm 0.1) \times 10^{17}$	8.14 ± 0.13	72.13 ± 0.06	$(6.8 \pm 1.1) \times 10^{17}$	11.6 ± 0.5	66.0 ± 0.2
G12.89+0.49	$(2.521 \pm 0.001) \times 10^{17}$	4.916 ± 0.004	33.004 ± 0.001	$(1.8863 \pm 0.0007) \times 10^{16}$	7.678 ± 0.003	32.286 ± 0.001
G16.57-0.05	$(4.51 \pm 0.01) \times 10^{16}$	6.51 ± 0.03	60.96 ± 0.01	$(1.524 \pm 0.007) \times 10^{15}$	4.32 ± 0.03	59.69 ± 0.01
G19.88-0.53 C1	$(4.67 \pm 0.02) \times 10^{16}$	5.43 ± 0.06	45.17 ± 0.02	$(1.123 \pm 0.002) \times 10^{16}$	6.97 ± 0.01	44.486 ± 0.006
G19.88-0.53 C2	$(9.36 \pm 0.04) \times 10^{15}$	3.59 ± 0.05	43.76 ± 0.02	$(6.82 \pm 0.04) \times 10^{14}$	5.36 ± 0.04	43.63 ± 0.01

Core	CH$_2$CHCN			CH$_3$CH$_2$CN		
	N (cm^{-2})	FWHM (km s^{-1})	V_{LSR} (km s^{-1})	N (cm^{-2})	FWHM (km s^{-1})	V_{LSR} (km s^{-1})
G9.62+0.19 C1	⋯	⋯	⋯	⋯	⋯	⋯
G9.62+0.19 C2	$(2.20 \pm 0.02) \times 10^{15}$	2.37 ± 0.04	2.69 ± 0.02	$(6.81 \pm 0.02) \times 10^{15}$	4.03 ± 0.01	2.042 ± 0.005
G9.62+0.19 C3	$(3.47 \pm 0.01) \times 10^{15}$	5.84 ± 0.05	5.82 ± 0.02	$(1.189 \pm 0.001) \times 10^{16}$	5.083 ± 0.006	5.678 ± 0.002
G10.47+0.03 (component 1)	$(5.63 \pm 0.12) \times 10^{17}$	9.02 ± 0.09	66.22 ± 0.01	$(6.01 \pm 0.17) \times 10^{16}$	7.6 ± 0.5	65.9 ± 0.1
G10.47+0.03 (component 2)	$(3.3 \pm 0.2) \times 10^{17}$	5.05 ± 0.07	67.42 ± 0.03	$(2.4 \pm 0.2) \times 10^{17}$	8.1 ± 0.4	67.1 ± 0.2
G12.89+0.49	$(2.45 \pm 0.03) \times 10^{15}$	8.50 ± 0.17	33.14 ± 0.06	$(8.029 \pm 0.009) \times 10^{15}$	5.130 ± 0.007	33.683 ± 0.003
G16.57-0.05	⋯	⋯	⋯	⋯	⋯	⋯
G19.88-0.53 C1	⋯	⋯	⋯	⋯	⋯	⋯
G19.88-0.53 C2	⋯	⋯	⋯	⋯	⋯	⋯

Notes. The errors indicate the standard deviation derived from the MCMC analysis. "⋯" means nondetection.
[a] The excitation temperature was fixed at 137 K.

Components 1 and 2 when we applied two-component fitting in the spectral analyses (Section 3.3).

Figure 14 shows a comparison of the chemical composition among each core. This figure suggests chemical diversity among MYSOs. The cores where we detected the HC$_5$N line are associated with all of the molecular species. For almost all of the species, the abundances with respect to CH$_3$CN vary by more than one order of magnitude among the cores, while the CH$_3$CH$_2$CN abundances show differences within a factor of ∼5. The CH$_2$CHCN abundance with respect to CH$_3$CN in G10.47+0.03 is higher than that of CH$_3$CH$_2$CN, which shows an opposite trend in the other cores.

We investigate the physical properties of sources between HC$_5$N-detected (G9.62+0.19, G10.47+0.03, and G12.89+0.49) and HC$_5$N-undetected (G16.57-0.05 and G19.88-0.53) sources. The physical properties derived by Urquhart et al. (2018), summarized in Table 1 of this paper, show similar values of T_{dust} and $N(H_2)$, which are most related to chemistry, among all of the five sources. However, Urquhart et al. (2018) derived these parameters for the same beam size, and then the

linear scales were different among each source due to different source distances. We then adopted modified blackbody models for a linear scale of 0.5 pc toward all of the sources, as explained in Appendix C. Figure 17 in Appendix C shows plots of infrared fluxes and the modified blackbody models which can reproduce the observed fluxes best, and Table 11 summarizes the fitting parameters.

The cold-component temperatures (T_c) are almost consistent within their errors among all of the sources except for G10.47+0.03 (Table 11). The luminosity (L) in G12.89+0.49 associated with the HC$_5$N emission is consistent with that in G16.57-0.05, where HC$_5$N has not been detected, within their errors. Thus, we cannot confirm the importance of luminosity for detection of HC$_5$N.

However, the different HC$_5$N abundances among the four cores (G9.62+0.19 C2, G9.62+0.19 C3, G10.47+0.03, and G12.89+0.49) by more than 1 order of magnitude may be related to the luminosity; G12.89+0.49 has the lowest HC$_5$N abundances and the lowest luminosity among the three sources. In contrast, the HC$_5$N abundance at G9.62+0.19 C2 is highest
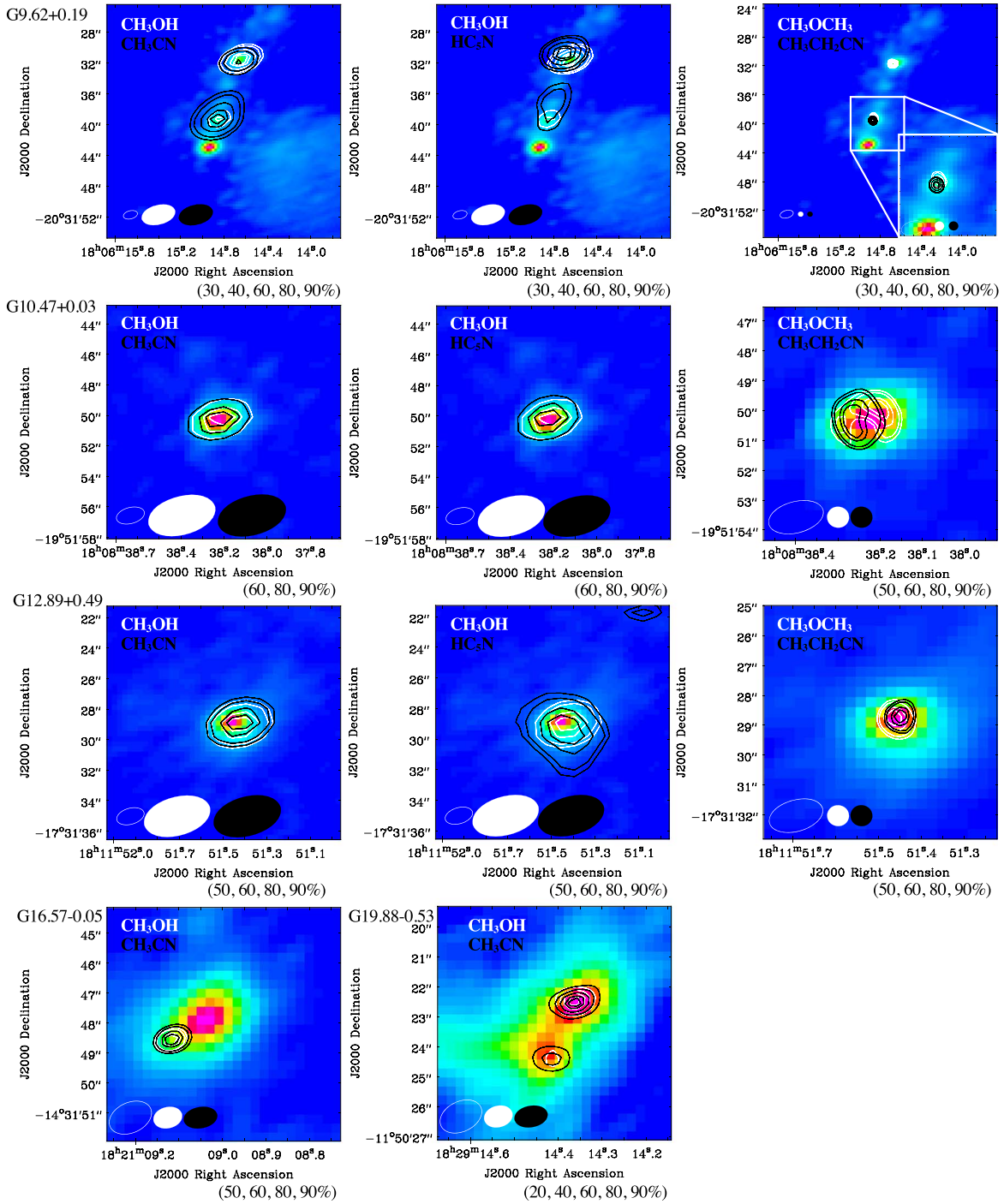
Figure 12. Comparison of spatial distributions among each species. The color scale shows the continuum image, the same as in Figure 1. The white and black contours show moment 0 maps of each species denoted at the top-left corners in each panel. The contour levels are relative values of the peak intensities, and the contour levels are indicated below each panel. Three panels of the first column, the second column, and the third column show comparisons in G9.62+0.19, G10.47+0.03, and G12.89 +0.49, respectively. The ellipses indicate the angular resolution: an open one corresponds to the continuum image, and white and black ones correspond to the moment 0 maps of each molecule. The colors are the same as the contours.

among the four cores. This core was proposed to be a late HMC or an HC H II region (Liu et al. 2017). If this source is an HC H II region, the UV radiation field should be stronger compared with the other cores. This implication may be consistent with the suggestion by Fontani et al. (2017): a high cosmic-ray ionization rate ($\zeta = 4 \times 10^{-14}$ s^{-1}) could explain their observational results of the higher HC_5N abundance with respect to HC_3N in the protoclusters OMC-2 FIR 4 and FIR 5. The inner density structure should be related to penetration of

energetic particles and photons, though we need higher-angular-resolution observations to confirm their effects. The nondetection of HC_5N at G9.62+0.19 C1, corresponding to an UC H II region (Liu et al. 2017), means that HC_5N may be efficiently destroyed at this evolutionary stage.

Although we cannot recognize significant differences in luminosity between the HC_5N-detected and HC_5N-undetected sources, the ratio of solid angles between warm and cold components (Ω_w/Ω_c) are more clearly different between them.
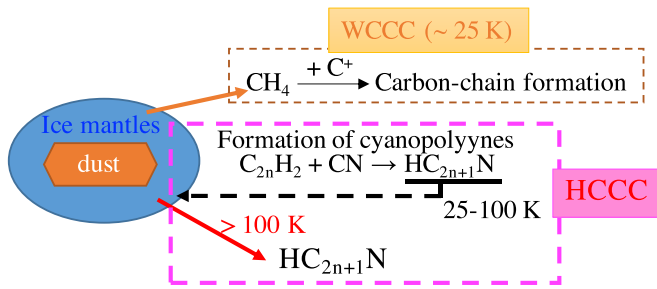
Figure 13. Warm carbon-chain chemistry (WCCC) and hot carbon-chain chemistry (HCCC). The HCCC mechanism was based on the chemical simulations by Taniguchi et al. (2019a).

We found that the HC$_5$N-detected sources have larger Ω_w/Ω_c ratios compared to the other group. Moreover, the temperatures of cold components are relatively higher in the HC$_5$N-detected sources. These results imply that the hot regions are likely more extended around MYSOs where HC$_5$N has been detected. This can be interpreted as that HC$_5$N and N-bearing COMs are detected from more evolved MYSOs. In summary, a hot region is likely important for detection of HC$_5$N around MYSOs, namely the HCCC mechanism (Figure 13), and moderate high dose of energetic photons or particles (e.g., UV radiation, cosmic rays) seems to further enhance the HC$_5$N abundance.

4.3. Comparison between Observational Results and Simulations

In this subsection, we will compare the results of observations and our chemical simulations. To simulate the abundances of the detected carbon-chain species, O-bearing and N-bearing COMs in the observed MYSOs, we have used the state-of-the-art three-phase chemical code Nautilus (Ruaud et al. 2016). Nautilus computes the time evolution of abundances of chemical species for a given set of physical conditions and chemical parameters. It simulates chemistry in the gas phase, grain surface, and grain mantle by considering various exchange processes such as adsorption of gas-phase species onto grain surfaces, the thermal and nonthermal desorption of species from grain surface into the gas phase, and the surface–mantle and mantle–surface exchange of species. Our gas-phase chemical network is based on the public chemical network kida.uva.2014 (Wakelam et al. 2015) with updates on chemistry of O-bearing and N-bearing COMs (Majumdar et al. 2018; Suzuki et al. 2018). The surface chemical network is based on the one from Garrod et al. (2007) with several additional processes and reactions (Ruaud et al. 2015; Majumdar et al. 2018; Suzuki et al. 2018).

To simulate the physical conditions in MYSOs, we have used the two-stage fast-warm-up model: freefall collapse, followed by a dynamically static warm-up stage (Garrod & Herbst 2006). The evolution of the physical parameters and initial elemental abundances were set at the same values as in Taniguchi et al. (2019a). In the freefall collapse stage, the temperature is kept at 10 K and the initial gas density is 10^4 cm^{-3}. The gas density increases to 10^7 cm^{-3} during the freefall collapse, which lasts for $\sim4.5 \times 10^5$ yr. According to the density increase, the visual extinction (A_v) increases from 5 to 500 mag. After the density reaches 10^7 cm^{-3}, the warm-up stage starts and the temperature rises from 10 to 200 K. The heating timescale is 5×10^4 yr, which represents a typical evolutionary timescale of formation of high-mass stars (Garrod & Herbst 2006). After the

temperature reaches 200 K at $\sim5.9 \times 10^5$ yr, the temperature is kept at 200 K until 10^7 yr (the hot-core stage). The temperature evolution is indicated as red dashed lines in Figure 15. The dust grain size is fixed at 0.1 μm. A cosmic-ray ionization rate (ζ) of 1.3×10^{-17} s^{-1} was adopted. We also run simulations with high cosmic-ray ionization rates (3.0×10^{-16} s^{-1} and 4.0×10^{-14} s^{-1}), as previous studies have done (Fontani et al. 2017; Taniguchi et al. 2019a). We find that models with higher cosmic-ray ionization rates cannot reproduce the observational results reasonably. Figure 18 in Appendix D shows comparisons of chemical simulations with three different cosmic-ray ionization rates. Here, we exclude these two results, and show results with $\zeta = 1.3 \times 10^{-17}$ s^{-1}.

Figure 15 shows comparisons of abundances between the observations (horizontal color lines) and the chemical simulations (black lines). Since our target sources include MYSOs, we focus on the warm-up and hot-core stages.

Figure 15(a) shows the time evolution of the HC$_5$N/CH$_3$CN abundance ratio. The observed HC$_5$N/CH$_3$CN abundance ratios agree with the simulation around $(4.45–4.51) \times 10^5$ yr and $(4.8–6.0) \times 10^5$ yr, and the corresponding temperature ranges are $\sim$12–19 K and $\sim$160–200 K, respectively. Here, we estimated the upper limit of line intensity of the observed HC$_5$N line under low-temperature ($T < 20$ K) conditions. In the estimation, the HC$_5$N column density is set at 1×10^{14} cm^{-2}. This column density was derived from the highest HC$_5$N abundance before the temperature reaches 20 K, including freefall collapse stage ($\simeq10^{-10}$ with respect to the number density of total hydrogen nuclei) and the assumed H$_2$ column density of 10^{24} cm^{-2}, which is a typical value in these high-mass star-forming regions (see Table 1). Other assumptions are as follows: $T_{ex} =$ 12–19 K, FWHM = 3 km s^{-1}, and no beam dilution. With these parameters, the observed HC$_5$N ($J = 35$ -34) line is not excited, and the upper limit of intensity of this HC$_5$N line is found to be $\sim$55 mK. This means that the HC$_5$N line should not have been detected in these data sets with noise levels around 0.2 K (Figure 8), if HC$_5$N exists in such low-temperature regions. Hence, the age of $(4.45–4.51) \times 10^5$ yr is not suitable for our target sources, and the most reasonable agreement between the observations and the simulation is $(4.8–6.0) \times 10^5$ yr ($T \approx$ 160–200 K). We also conducted the same test for the other molecular lines described above, and constrained the ages in which the modeled abundance ratios agree with the observed ones. Low-temperature conditions (<100 K) are rejected for all of the molecules. In the following parts, we mention only the best chemical ages which are constrained by these tests.

At $(4.8–6.0) \times 10^5$ yr ($T \approx$ 160–200 K), both CH$_3$CN and HC$_5$N sublimate from dust grains into the gas phase by the thermal desorption mechanism. The HC$_5$N molecules are formed in the gas phase, adsorbed onto dust grains, and accumulated in ice mantles during the starless-core and warm-up stages before the temperature reaches its sublimation temperature ($\sim$100 K). Hence, we conclude that the HC$_5$N detected around MYSOs comes from dust grains, and exists in the hot-core regions ($T > 100$ K). These results confirm that cyanopolyyne chemistry around MYSOs cannot be explained by WCCC, and we need HCCC (see Figure 13). Regarding CH$_3$CN, the dust–surface radical–radical reaction between NH and H$_2$CCN produces the gas-phase CH$_3$CN, which is adsorbed onto dust grains again, in the starless-core stage and warm-up
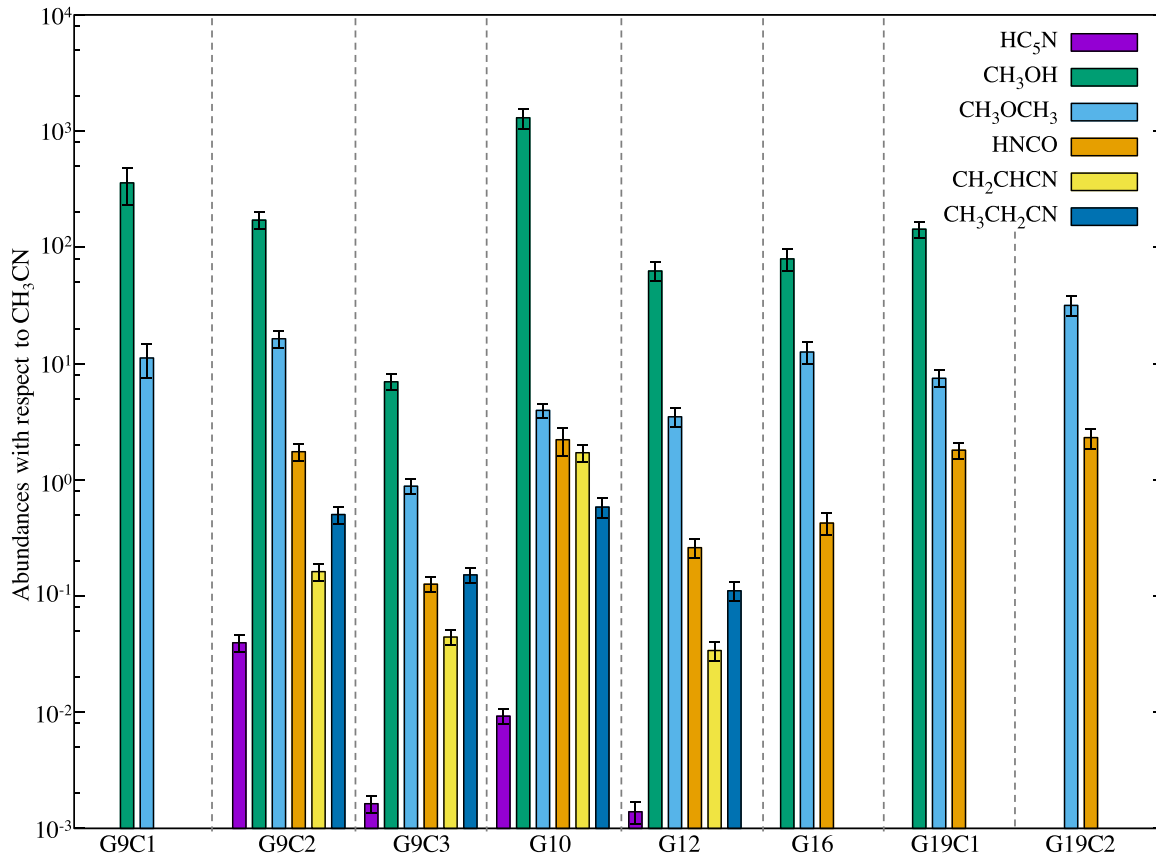
Figure 14. Comparison of chemical compositions with respect to CH_3CN.

stage before the temperature reaches its sublimation temperature ($\sim$100 K).

Figure 15(b) shows results of the CH_3OH/CH_3CN abundance ratios. The observed abundance ratios toward all of the sources can be reproduced by the simulation around 6.54×10^5–1.1×10^6 yr ($T = 200$ K). The CH_3OH molecules sublimate from dust grains via the thermal desorption mechanism, namely hot-core chemistry. These CH_3OH molecules coming from dust grains are formed in the starless-core stage; the CH_3OH molecules are formed by the dust–surface reaction between CH_3NH_2 and CH_3O to produce CH_3OH and CH_2NH_2. Some fractions of the formed two molecules desorb into the gas phase, and others remain on dust surfaces.

Figure 15(c) shows the CH_3OCH_3 case. The observations and simulation agree around 6.5×10^5–1.16×10^6 yr ($T = 200$ K). During these ages, the thermal sublimation of CH_3OCH_3 is the most dominant production pathway. In the starless-core stage, this molecule is formed in ice mantle by the association reaction between CH_3 and CH_3O, and the formed CH_3OCH_3 molecules move to dust surfaces or gas phase so that the equilibrium state realizes. The two O-bearing COMs can be reproduced around similar ages (6.5×10^5–1.1×10^6 yr) with a temperature of 200 K, implying that both of the species are produced by the hot-core chemistry.

Panel (d) shows the results of HNCO. We found that the observed $HNCO/CH_3CN$ abundance ratios cannot be reproduced during the warm-up and hot-core stages, but marginally agree with the low-temperature regime ($T \approx 12$ K), which is unlikely for our target sources. This may mean that HNCO is significantly affected by the shock chemistry, which we did not

take into consideration in the chemical simulation. In fact, Burkhardt et al. (2019) showed that the HNCO abundance is strongly enhanced during the sputtering and redeposition regimes. We have already mentioned the possibility that the HNCO emission comes from outflows in Section 4.1.

Figures 15(e) and (f) show the results of CH_2CHCN and CH_3CH_2CN, respectively. The observed CH_2CHCN/CH_3CN abundance ratios can be reproduced around $(4.8$–$7.2) \times 10^5$ yr, when temperatures are $\sim$140–200 K, and the CH_3CH_2CN/CH_3CN abundance ratios agree with the simulation around $(7$–$8) \times 10^5$ yr ($T = 200$ K). Regarding CH_2CHCN, its thermal sublimation is responsible for reproduction of the observed abundances. CH_2CHCN is formed in the gas phase in the starless-core stage by the reaction of "$CN + C_2H_4 \rightarrow CH_2CHCN + H$" and the electron recombination reactions of $C_2H_4CN^+$ and $C_3H_3NH^+$. The formed CH_2CHCN molecules are adsorbed onto dust grains and accumulated in ice mantles.

Formation of CH_3CH_2CN is not efficient in the starless-core stage, and it can be efficiently formed in the warm-up stage. The CH_3CH_2CN abundance steeply increases at $\sim$4.62 $\times 10^5$ yr ($T \approx 47$ K). At that time, this molecule is efficiently formed by "$JH + JCH_3CHCN \rightarrow CH_3CH_2CN$," where "$J$" denotes species on the dust surface. During the age when the observations and simulation agree ($\sim$7 $\times 10^5$ yr), the most dominant formation pathway in our simulation is the following gas-phase reaction:

$$HCO + CH_3CHCN \rightarrow CH_3CH_2CN + CO. \qquad (1)$$

This reaction becomes dominant from $\sim$4.88 $\times 10^5$ yr, when the temperature reaches around 190 K, to 1.05×10^6 yr ($T = 200$ K). In summary, the observed abundances of the N-bearing COMs best agree with the simulation around 7×10^5 yr.
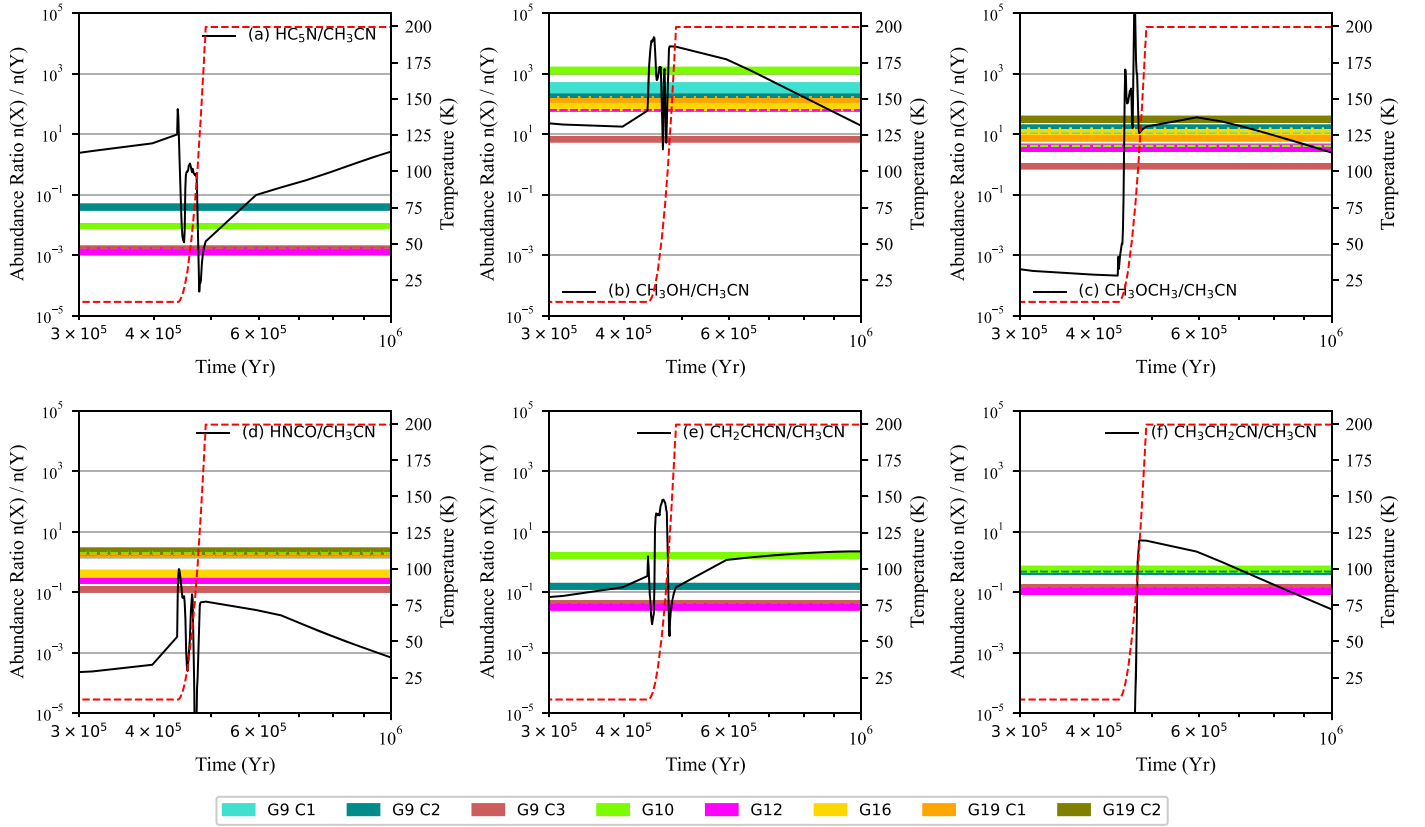
Figure 15. Comparison between the observed molecular abundances with respect to CH_3CN at each core (horizontal color lines) and the modeled ones (black solid lines). The red dashed lines indicate the temperature evolution.

We found that the observed abundances of all of the molecules, except for HNCO, toward the five MYSOs can be explained by the hot-core stage when the temperature exceeds 100 K. Although the best agreement ages are $(\sim 6\text{--}7) \times 10^5$ yr, the important point is not the absolute age but the corresponding temperature. All of the observed molecular abundances, except for HNCO, agree with the model at the temperature between 160 and 200 K. These results support the HCCC mechanism, which is necessary for reproducing the observed HC_5N abundances around MYSOs.

5. Conclusions

We present ALMA Band 3 data of the carbon-chain species and COMs toward the five MYSOs, and demonstrate chemical simulations of hot-core models with a warm-up stage. We investigate the relationships between carbon-chain species and COMs around the MYSOs with spatially resolved data, and the relationships between chemical composition and physical conditions. The main conclusions of this paper are as follows:

1. The HC_5N ($J = 35-34$) line has been detected from the three MYSOs where the N-bearing COMs (CH_2CHCN and CH_3CH_2CN) have been detected. The HC_5N line shows compact emission associated with the continuum core. Its spatial distributions are consistent with those of COMs, which implies that the HC_5N line comes from hot-core regions with temperatures above 100 K. On the other hand, the CCH emission is depleted at the continuum core and hot-core regions.

2. We do not find clear evidence for the chemical differentiation between O-bearing COMs and N-bearing COMs with the current ang. res. In G10.47+0.03, the CH_3OCH_3 emission shows a ring-like distribution and a double-peaked feature in its spectrum, suggestive of an expanding shell or an accretion disk shock. On the other hand, the emission of the other molecules does not show such features.

3. We derive physical parameters within 0.5 pc by the two-temperature modified blackbody model, and investigate the relationship with chemical composition. We did not recognize any clear difference in temperature and bolometric luminosity between the three MYSOs associated with the HC_5N emission and the other two MYSOs without it. The solid-angle ratios between warm and cold components (Ω_w/Ω_c) are higher in the MYSOs associated with HC_5N and N-bearing COMs. These results indicate that the hot regions are much extended around the MYSOs where HC_5N and N-bearing COMs have been detected.

4. The observed molecular abundances with respect to CH_3CN around the target MYSOs agree with the chemical simulations around $(6\text{--}7) \times 10^5$ yr, at which the temperature reaches 200 K, namely the hot-core chemistry phase. These results support that the HC_5N emission comes from the hot-core regions with temperatures above 100 K. In such high-temperature regions, radical-type carbon-chain species (e.g., CCH) are predicted to be efficiently destroyed in the gas phase. This can be seen in the moment 0 maps, because the CCH emission is

depleted at the peaks of the HC_5N and COMs emission, as well as the continuum emission.

5. We propose *hot carbon-chain chemistry (HCCC)* to explain the observed features of the carbon-chain species around MYSOs. In HCCC, cyanopolyynes ($HC_{2n+1}N$) sublimate from dust grains with temperatures above 100 K, while the radical-type species are deficient in such hot regions. The HCCC mechanism and hot-core chemistry, which is rich with COMs, could occur simultaneously, and they are not mutually exclusive.

Appendix A
Molecular Lines Optical Depth

Table 9 summarizes the optical depths of the CH_3CN lines for the best-fit models derived by the MCMC method.

Table 9
Optical Depths of the CH_3CN Lines

Lines	G9.62+0.19 C1	G9.62+0.19 C2	G9.62+0.19 C3	G10.47+0.03	G12.89+0.49	G16.57-0.05	G19.88-0.53 C1	G19.88-0.53 C2
$K = 0$	0.067	0.039	0.366, 2.21	0.300, 11.75	5.24, 3.14	0.134	0.067	0.039
$K = 1$	0.062	0.035	0.331, 1.99	0.282, 10.71	4.69, 2.81	0.122	0.062	0.035
$K = 2$	0.049	0.024	0.242, 1.44	0.221, 8.02	3.33, 1.98	0.091	0.049	0.024
$K = 3$[a]	0.064	0.024	0.274, 1.596	0.280, 5.42	3.58, 2.12	0.106	0.064	0.024

Notes. In the cases where two values are listed, they are values for "component 1" and "component 2," respectively.

[a] The $K = 3$ transition has degeneracy ($K = -3 \rightarrow 3$ and $3 \rightarrow -3$). The optical depths of these two transitions are the same. The listed values are the sum of these two degenerate transitions.

Appendix B
Channel Maps of CH_3OCH_3 in G10.47+0.03

Figure 16 shows channel maps of the CH_3OCH_3 line toward G10.47+0.03. In the highly redshifted velocity range (76–75 km s^{-1}), the emission is located only toward the northwest, while emission of lower-velocity components is also present toward the northeast, east, and southeast. In the highly blueshifted velocity range (59–58 km s^{-1}), the emission is again located to the northwest only. A rotating and expanding shell motion plus skewed emission distribution toward the northwest could reproduce the observed velocity structure.

Detailed analysis using our model will be discussed in a future paper.

Appendix C
Modified Blackbody Model

We adopted a two-component modified blackbody model (or two-component radiative-transfer model) for all of the five target sources, using archival data from Spitzer[17] (3.6, 4.5, and 8 μm) and Herschel[18] (70, 160, 250, 350, and 500 μm). Using these infrared archival data, we obtained flux density values with 0.5 pc in diameter toward all of the sources: 19''83, 9''62, 34''38, 21''92, and 31''25 for G9.62+0.19, G10.47+0.03,
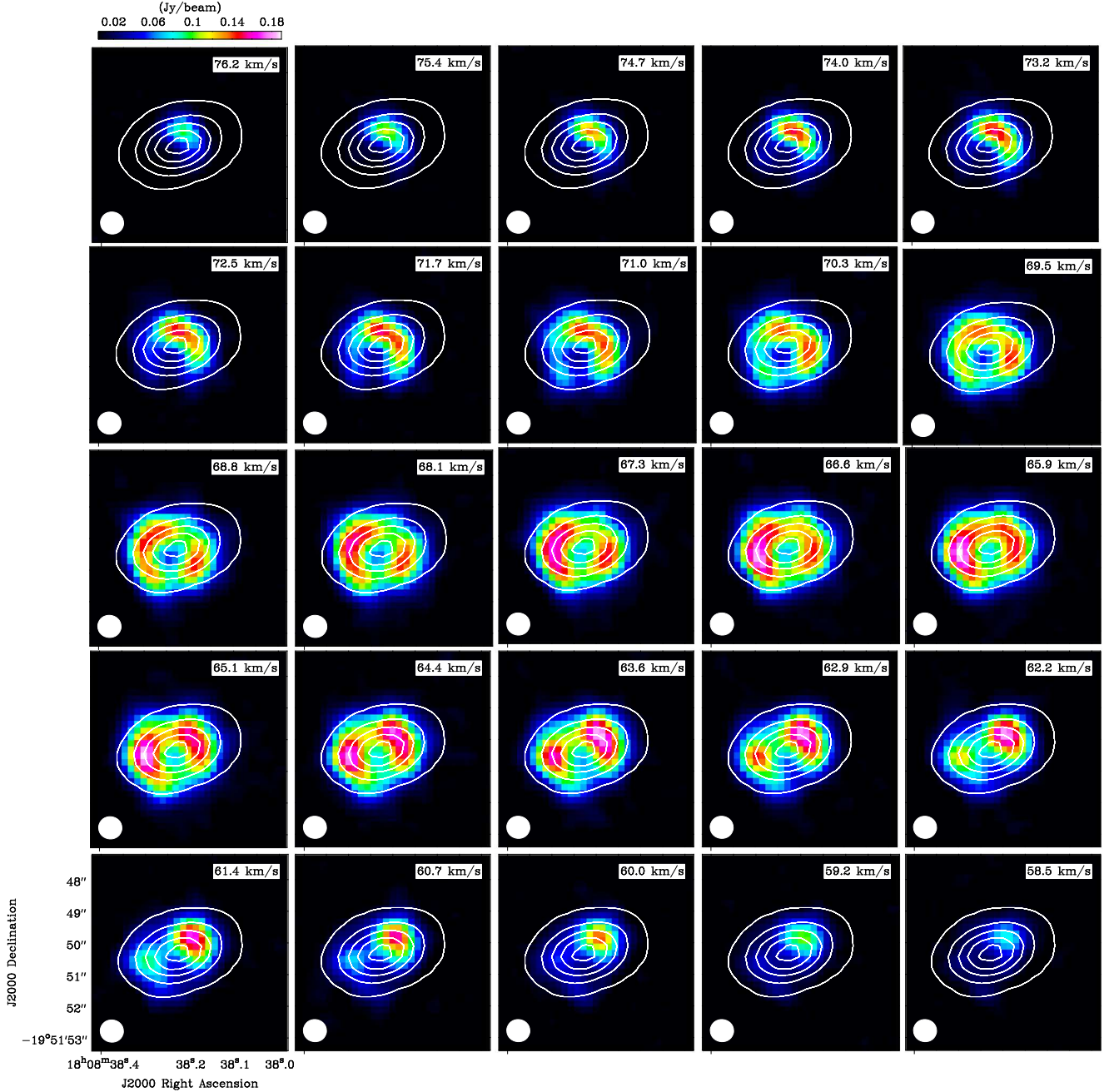
Figure 16. Channel maps of CH_3OCH_3 in G10.47+0.03. The white contours indicate the continuum emission (from 20σ to 180σ in 40σ step).

[17] https://irsa.ipac.caltech.edu/frontpage/
[18] http://archives.esac.esa.int/hsa/whsa/

Table 10
Flux Density at Each Wavelength

Source	3.6 μm	4.5 μm	8 μm	70 μm	160 μm	250 μm	350 μm	500 μm
G9.62+0.19	3.9 (0.9) × 10^{-4}	0.40 (0.08)	3.1 (0.6)	2037 (818)	1688 (661)	411 (154)	265 (133)	78 (45)
G10.47+0.03	7.7 (2.1) × 10^{-5}	0.049 (0.010)	0.72 (0.14)	970 (564)	578 (337)	110 (64)	112 (87)	22 (11)
G12.89+0.49	8.1 (2.3) × 10^{-4}	0.89 (0.18)	3.5 (0.7)	1262 (460)	1509 (504)	704 (234)	348 (139)	104 (46)
G16.57-0.05	2.1 (0.5) × 10^{-4}	0.15 (0.03)	1.7 (0.3)	380 (155)	491 (188)	322 (122)	138 (64)	35 (19)
G19.88-0.53	5.1 (1.3) × 10^{-4}	0.59 (0.12)	2.3 (0.5)	337 (123)	675 (229)	409 (143)	198 (82)	61 (29)

Note. Unit is janskys. The values in parentheses are uncertainties. These errors were calculated from the rms noise levels of images, and we included an assumed 20% absolute calibration error.

G12.89+0.49, G16.57-0.05, and G19.88-0.53, respectively. The coordinates of the central positions of these analyses are summarized in Table 1. Table 10 summarizes the obtained flux density values at each frequency. We estimated uncertainties of the flux densities including an assumed 20% calibration error and rms noise levels of archival images calculated in CASA.

We assume that the emission of 250 μm (1.199169832 THz) is optically thin, and used fluxes at this wavelength as a reference. We calculated the optical depths of other wavelengths using the following formula:

$$\tau_\nu = \tau(250\,\mu\mathrm{m})\left(\frac{\nu}{1.199169832\,\mathrm{THz}}\right)^\beta. \tag{C1}$$

The spectral index (β) was treated as a free parameter with a range of 1.0–2.4 (Rigby et al. 2018). We searched for the best β values for each source by changing this parameter in steps of 0.05; $\beta = 1.5$ for all of the sources except for G19.88-0.53, where $\beta = 1.75$ is applied. Since the emission regions of the warm components should be smaller than those of the cold components, we multiplied the warm component by $\Omega_w/\Omega c$ (Ω is solid angle) to correct this effect. We searched for the best combination of three

Table 11
Physical Parameters Derived from Fitting by the Modified Blackbody Model

Source	T_c (K)	T_w (K)	Ω_w/Ω_c	L ($L_\odot$)
G9.62+0.19	29 ± 3	150 ± 5	(5.0 ± 0.2) × 10^{-6}	(1.4 ± 0.2) × 10^6
G10.47+0.03	40 ± 4	150 ± 5	(5.0 ± 0.2) × 10^{-6}	(2.1 ± 0.4) × 10^6
G12.89+0.49	25 ± 3	150 ± 5	(1.0 ± 0.2) × 10^{-6}	(3.7 ± 0.5) × 10^5
G16.57-0.05	23 ± 3	160 ± 5	(4 ± 1) × 10^{-7}	(2.6 ± 0.4) × 10^5
G19.88-0.53	22 ± 3	160 ± 5	(3 ± 1) × 10^{-7}	(1.5 ± 0.3) × 10^5

free parameters (T_c, T_w, Ω_w/Ω_c), changing with steps of 1 K, 5 K, and 1×10^{-7} for T_c, T_w, and Ω_w/Ω_c, respectively.

Figure 17 shows the modified blackbody models which reproduce the observed flux values best. Table 11 summarizes the results including total luminosities derived from the results of the best blackbody models, i.e., $L = 4\pi d^2 \int S_\nu d\nu$. The adopted source distances (d) are summarized in Table 1. The obtained values here are different from Urquhart et al. (2018) because of different areas. The source luminosities derived by our method are typical for MYSOs.
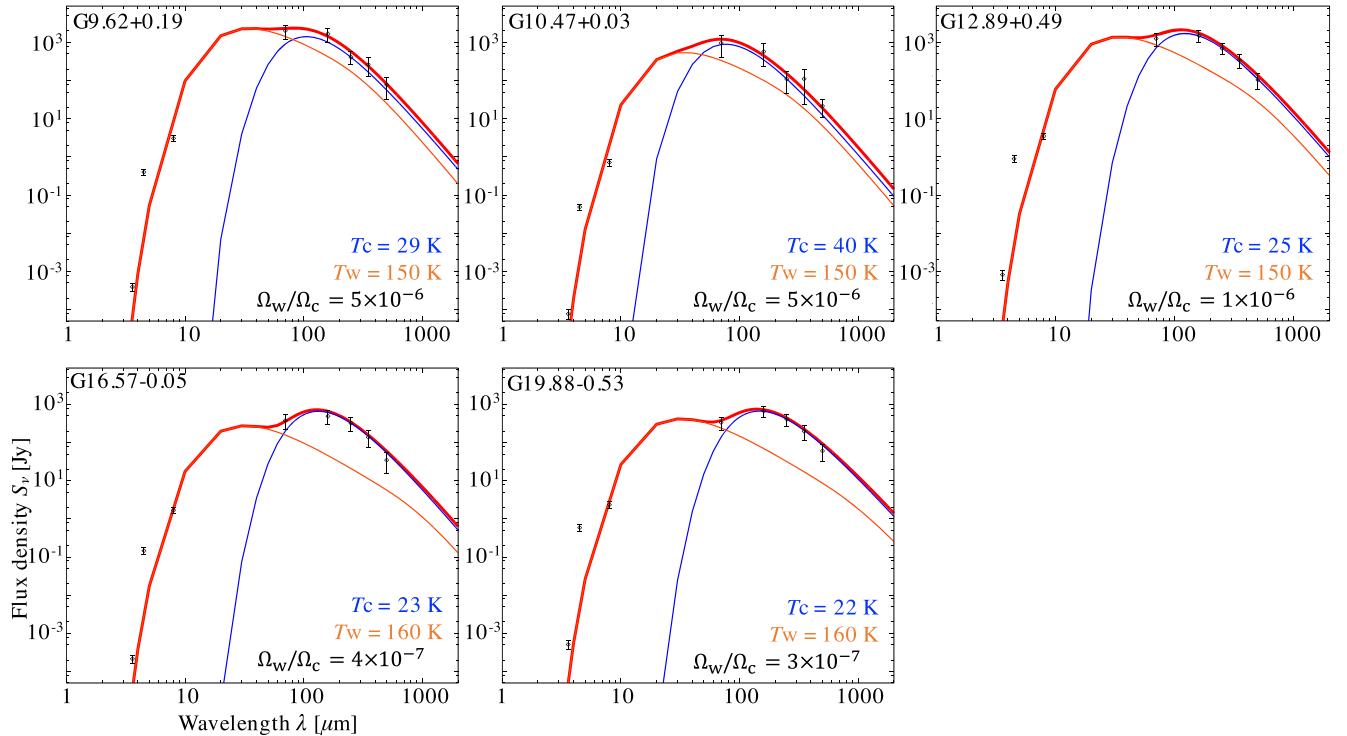

Figure 17. Plots of infrared fluxes and the modified blackbody models which can reproduce the observed fluxes best. Blue and orange curves indicate cold and warm components, respectively. Red curves show sums of the cold and warm components. Black points are data points taken from the archival data. T_c and T_w indicate temperatures of cold and warm components, respectively. Ω_w/Ω_c indicates applied solid-angle ratios between warm and cold components.

Appendix D
Comparisons of Model Results with Different Cosmic-ray Ionization Rates

Figure 18 shows comparisons of abundances with respect to CH_3CN derived by chemical simulations with three different cosmic-ray ionization rates. Abundance ratios of O-bearing COMs (CH_3OH and CH_3OCH_3) and CH_2CHCN with respect to

CH_3CN are lower in models with two higher cosmic-ray ionization rates. The HC_5N/CH_3CN abundance ratio with $\zeta = 3.0 \times 10^{-16}$ s^{-1} is much higher compared to the other two models. Details of cyanopolyyne chemistry in different cosmic-ray ionization rates were explained in Taniguchi et al. (2019a). These models with the two higher cosmic-ray ionization rates cannot reproduce the observed abundance ratios simultaneously.
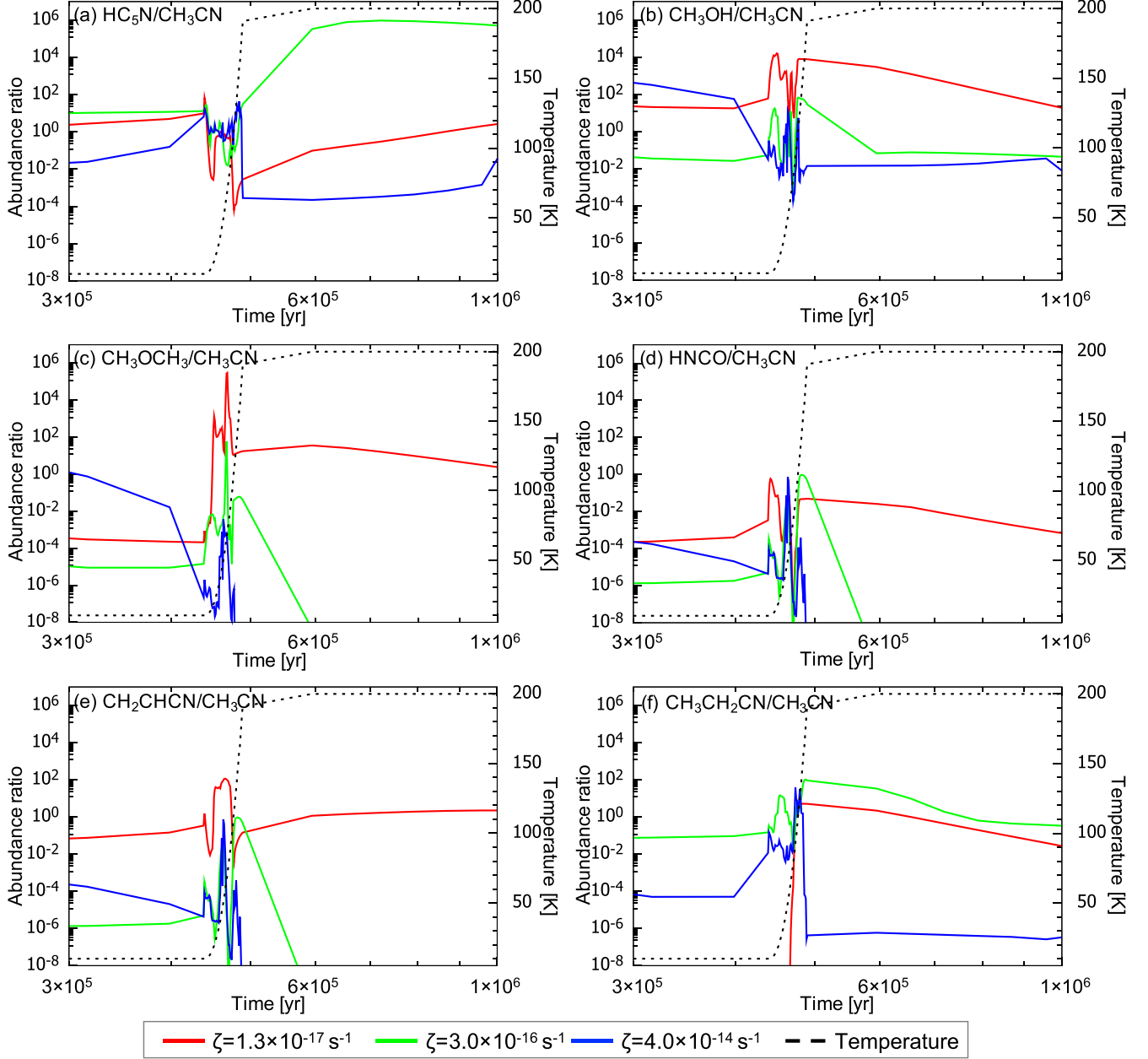

Figure 18. Comparisons of results obtained by chemical simulations with three different cosmic-ray ionization rates (red: 1.3×10^{-17} s^{-1}, green: 3.0×10^{-16} s^{-1}, blue: 4.0×10^{-14} s^{-1}). The black dashed curves indicate the temperature.

ORCID iDs

Kotomi Taniguchi ● https://orcid.org/0000-0003-4402-6475
Liton Majumdar ● https://orcid.org/0000-0001-7031-8039
Paola Caselli ● https://orcid.org/0000-0003-1481-7911
Shigehisa Takakuwa ● https://orcid.org/0000-0003-0845-128X
Tien-Hao Hsieh ● https://orcid.org/0000-0002-5507-5697
Masao Saito ● https://orcid.org/0000-0003-0769-8627
Zhi-Yun Li ● https://orcid.org/0000-0002-7402-6487
Kazuhito Dobashi ● https://orcid.org/0000-0001-8058-8577
Tomomi Shimoikura ● https://orcid.org/0000-0002-1054-3004
Fumitaka Nakamura ● https://orcid.org/0000-0001-5431-2294
Jonathan C. Tan ● https://orcid.org/0000-0002-3389-9142
Eric Herbst ● https://orcid.org/0000-0002-4649-2536

References

Benson, P. J., Caselli, P., & Myers, P. C. 1998, ApJ, 506, 743
Burkhardt, A. M., Shingledecker, C. N., Le Gal, R., et al. 2019, ApJ, 881, 32
Caselli, P., & Ceccarelli, C. 2012, A&ARv, 20, 56
Csengeri, T., Belloche, A., Bontemps, S., et al. 2019, A&A, 632, A57
Endres, C. P., Schlemmer, S., Schilke, P., et al. 2016, JMoSp, 327, 95
Fontani, F., Ceccarelli, C., Favre, C., et al. 2017, A&A, 605, A57
Garrod, R. T., & Herbst, E. 2006, A&A, 457, 927
Garrod, R. T., Wakelam, V., & Herbst, E. 2007, A&A, 467, 1103
Gieser, C., Beuther, H., Semenov, D., et al. 2023, arXiv:2304.07237
Gorai, P., Bhat, B., Sil, M., et al. 2020, ApJ, 895, 86
Gorai, P., Das, A., Shimonishi, T., et al. 2021, ApJ, 907, 108
Graninger, D. M., Wilkins, O. H., & Öberg, K. I. 2016, ApJ, 819, 140
Green, C.-E., Green, J. A., Burton, M. G., et al. 2014, MNRAS, 443, 2252
Hassel, G. E., Herbst, E., & Garrod, R. T. 2008, ApJ, 681, 1385
Herbst, E., & Leung, C. M. 1989, ApJS, 69, 271
Herbst, E., & van Dishoeck, E. F. 2009, ARA&A, 47, 427
Higuchi, A. E., Sakai, N., Watanabe, Y., et al. 2018, ApJS, 236, 52
Issac, N., Tej, A., Liu, T., et al. 2020, MNRAS, 497, 5454
Jørgensen, J. K., Belloche, A., & Garrod, R. T. 2020, ARA&A, 58, 727
Lindberg, J. E., Charnley, S. B., Jørgensen, J. K., et al. 2017, ApJ, 835, 3
Liu, T., Lacy, J., Li, P. S., et al. 2017, ApJ, 849, 25
Majumdar, L., Loison, J.-C., Ruaud, M., et al. 2018, MNRAS, 473, L59
McMullin, J. P., Waters, B., Schiebel, D., et al. 2007, in ASP Conf. Proc. 376, Astronomical Data Analysis Software and Systems XVI, ed. R. A. Shaw et al. (San Francisco, CA: ASP), 127
Müller, H. S. P., Schlöder, F., Stutzki, J., et al. 2005, JMoSt, 742, 215
Qin, S.-L., Liu, T., Liu, X., et al. 2022, MNRAS, 511, 3463
Rigby, A. J., Peretto, N., Adam, R., et al. 2018, A&A, 615, A18
Rivilla, V. M., Colzi, L., Fontani, F., et al. 2020, MNRAS, 496, 1990
Rodríguez-Garza, C. B., Kurtz, S. E., Gómez-Ruiz, A. I., et al. 2017, ApJS, 233, 4
Ruaud, M., Loison, J. C., Hickson, K. M., et al. 2015, MNRAS, 447, 4004
Ruaud, M., Wakelam, V., & Hersant, F. 2016, MNRAS, 459, 3756
Sakai, N., Sakai, T., Hirota, T., et al. 2008, ApJ, 672, 371
Sanhueza, P., Girart, J. M., Padovani, M., et al. 2021, ApJL, 915, L10
Suzuki, H., Yamamoto, S., Ohishi, M., et al. 1992, ApJ, 392, 551
Suzuki, T., Ohishi, M., Saito, M., et al. 2018, ApJS, 237, 3
Taniguchi, K., Guzmán, A. E., Majumdar, L., et al. 2020, ApJ, 898, 54
Taniguchi, K., Herbst, E., Caselli, P., et al. 2019a, ApJ, 881, 57
Taniguchi, K., Herbst, E., Majumdar, L., et al. 2021a, ApJ, 908, 100
Taniguchi, K., Majumdar, L., Plunkett, A., et al. 2021b, ApJ, 922, 152
Taniguchi, K., Miyamoto, Y., Saito, M., et al. 2018a, ApJ, 866, 32
Taniguchi, K., Saito, M., Hirota, T., et al. 2017, ApJ, 844, 68
Taniguchi, K., Saito, M., Majumdar, L., et al. 2018b, ApJ, 866, 150
Taniguchi, K., Saito, M., Sridharan, T. K., et al. 2018c, ApJ, 854, 133
Taniguchi, K., Saito, M., Sridharan, T. K., et al. 2019b, ApJ, 872, 154
Urquhart, J. S., König, C., Giannetti, A., et al. 2018, MNRAS, 473, 1059
Vastel, C., Bottinelli, S., Caux, E., et al. 2015, in SF2A-2015: Proc. Annual Meeting of the French Society of Astronomy and Astrophysics (Paris: Société astronomique de France), 313
Wakelam, V., Loison, J.-C., Herbst, E., et al. 2015, ApJS, 217, 20
Zapata, L. A., Rodríguez, L. F., Ho, P. T. P., et al. 2006, AJ, 131, 939